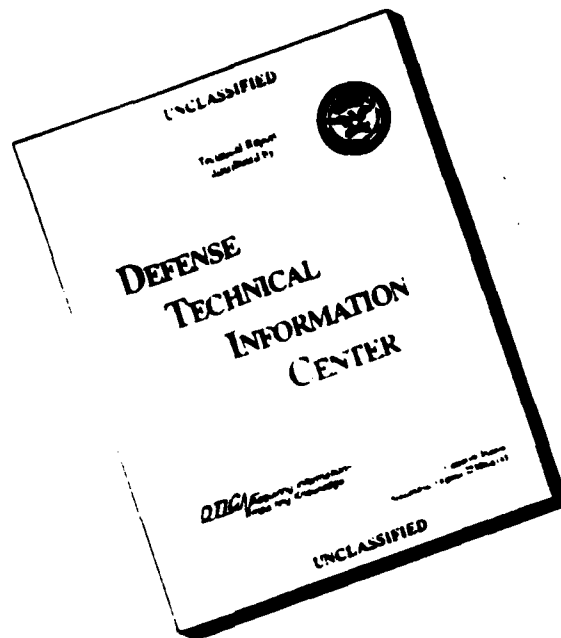


DISCLAIMER NOTICE



THIS REPORT IS INCOMPLETE BUT IS THE BEST AVAILABLE COPY FURNISHED TO THE CENTER. THERE ARE MULTIPLE MISSING PAGES. ALL ATTEMPTS TO DATE TO OBTAIN THE MISSING PAGES HAVE BEEN UNSUCCESSFUL.

ADA 279662

**MASSACHUSETTS INSTITUTE OF TECHNOLOGY
LINCOLN LABORATORY**

SOLID STATE RESEARCH

QUARTERLY TECHNICAL REPORT

1 MAY — 31 JULY 1993

ISSUED 18 FEBRUARY 1994

Approved for public release; distribution is unlimited.

DTIC QUALITY INSPECTED 5

LEXINGTON

MASSACHUSETTS

ABSTRACT

This report covers in detail the research work of the Solid State Division at Lincoln Laboratory for the period 1 May through 31 July 1993. The topics covered are Electrooptical Devices, Quantum Electronics, Materials Research, Submicrometer Technology, High Speed Electronics, Microelectronics, and Analog Device Technology. Funding is provided primarily by the Air Force, with additional support provided by the Army, ARPA, Navy, SDIO, and NASA.

Accession For	
NTIS GRA&I	<input checked="checked" type="checkbox"/>
DTIC TAB	<input type="checkbox"/>
Unannounced	<input type="checkbox"/>
Justification	
By	
Distribution	
Availability Codes	
Dist	Avail and/or Special
A-1	

TABLE OF CONTENTS

Abstract	iii
List of Illustrations	vii
List of Tables	x
Introduction	xi
Reports on Solid State Research	xiii
Organization	xxiii
 1. ELECTROOPTICAL DEVICES	 1
1.1 Effect of Annealing on Photorefractive Damage in Ti-Indiffused LiNbO ₃ Modulators	 1
 2. QUANTUM ELECTRONICS	 5
2.1 High-Power GaSb-Based Lasers Emitting at 3–4 μm	5
 3. MATERIALS RESEARCH	 9
3.1 Single-Frequency GaInAsSb/AlGaAsSb Quantum-Well Ridge-Waveguide Lasers Emitting at 2.1 μm	 9
3.2 GaInAsSb/AlGaAsSb Tapered Lasers Emitting at 2 μm	11
3.3 Growth of InAs on GaAs Substrates by Organometallic Vapor Phase Epitaxy	15
 4. SUBMICROMETER TECHNOLOGY	 21
4.1 Simulation of Sub-0.25- μm Resist Processes for 193-nm Lithography	21
4.2 Evaluation of Depth of Focus in Photolithography at 0.25 μm	24
 5. HIGH SPEED ELECTRONICS	 29
5.1 Qualitative Model for the Current Stability of Hydrogen-Passivated Molybdenum Field-Emission Cones	29
 6. MICROELECTRONICS	 35
6.1 Modeling of Charge Packet Diffusion in the Field-Free Region of a Thinned Back-Illuminated Charge-Coupled Device	35
 7. ANALOG DEVICE TECHNOLOGY	 39
7.1 Test Circuit for Dual-Analog-Ternary Correlator	39
7.2 High-Power-Handling YBCO Films	43

LIST OF ILLUSTRATIONS

Figure No.		Page
1-1	Phase bias drift in modulators annealed twice for 7 h at 500°C in wet oxygen. No photorefractive-related decrease in optical transmission occurred during these tests. (Gaps in the data are due to recording failures; the optical power remained on.)	3
1-2	Result of photoconductive test with 90 mW at 1064 nm. The dc bias voltage was controlled to maintain a constant modulator phase bias. The V_{π} was 1.1 V for this device.	3
2-1	Power output of GaInAsSb/GaSb laser pumped with 0.8- μ m diode array: (a) peak power at 0.08% duty cycle for various temperatures, and (b) peak and maximum average power for various duty cycles at 85 K.	6
2-2	Power output of InAsSb/GaSb laser pumped with 0.94- μ m diode array: (a) peak power at 0.08% duty cycle for various temperatures, and (b) peak and maximum average power for various duty cycles at 85 K.	7
3-1	Schematic of ridge-waveguide laser. The width of the ridge is 8 μ m.	9
3-2	Light output vs current for GaInAsSb/AlGaAsSb ridge-waveguide laser under CW operation. The cavity length is 1000 μ m and reflectivities for back and front facets are 95 and 3%, respectively.	10
3-3	Emission spectrum of GaInAsSb/AlGaAsSb ridge-waveguide laser at 130 mA dc.	11
3-4	Schematic of tapered oscillator showing cavity-spoiling grooves, tapered gain region, and dimensions of input and output apertures.	12
3-5	Light output vs current of GaInAsSb/AlGaAsSb tapered oscillator. The central-lobe power is indicated by dots.	13
3-6	Far-field pattern of GaInAsSb/AlGaAsSb tapered oscillator at three current levels.	14
3-7	Dependence of InAs growth rate on substrate temperature.	16
3-8	Electron concentration and mobility of InAs layers at 77 K as a function of (a) growth temperature and (b) V/III ratio.	17
3-9	Normalized photoluminescence peak intensity of InAs layers as a function of (a) growth temperature and (b) V/III ratio.	18

LIST OF ILLUSTRATIONS (Continued)

Figure No.		Page
4-1	Cross-sectional scanning electron micrograph of oversilylated nominally 1.0- μm line-and-space structure imaged in poly(vinylphenol) at 193 nm. The silylation time was 5 min compared to a normal silylation time of 1–2 min. Note evidence of lateral diffusion by the silylating agent, which narrows the unsilylated width. The apparent silylation in the unsilylated area is a combination of gold (40 nm) deposited to prevent specimen charging in the electron microscope and a small amount of silylation (10–20 nm).	22
4-2	Comparison of MOSES silylation model (dashed line) with an experimentally measured silylation profile (solid line). The resist was poly(vinylphenol), the simulated exposure dose was 80 mJ/cm ² , and the silylation conditions were 105°C, 1.5 min, 10 Torr. The model assumed diffraction-limited optics, whereas the experimental image quality was limited by aberrations. The differences in aerial image may account for the differences in profile. For the experimental exposure, the fluence per pulse was calibrated at ~ 0.25 mJ/cm ² per pulse.	23
4-3	Exposure-defocus (E-D) plots of aerial image of equal lines and spaces, an isolated line, and an isolated contact hole, representing exposure (a) at 193 nm with 0.5 numerical aperture (NA) and coherence factor $\sigma = 0.6$, and (b) at 248 nm with 0.65 NA and $\sigma = 0.6$. The nominal feature size was 0.25 μm , and a $\pm 10\%$ linewidth control was used throughout. The dose values were normalized to that required for open field exposure. The usable E-D parameter space for each feature type is enclosed between its two corresponding lines and the x-axis.	25
4-4	Calculated depth of focus (DOF) of the aerial image of 0.25- μm equal lines and spaces, as a function of NA of the exposure tool. Two wavelengths are used in the simulation, 193 and 248 nm, each under two illumination conditions: circular with $\sigma = 0.6$, and annular with inner and outer radii, respectively, of 0.4 and 0.6, normalized to the maximum viewable source size.	26
4-5	Calculated DOF of the aerial image of 0.25- μm isolated contact hole. The exposure conditions are as in Figure 4-4.	27
5-1	Schematic diagrams of nonhydrogenated tips. (a) Tip during low-current operation. At low current levels the structure is stable even though some surface contaminants diffuse into the grains. (b) Tip during high-current operation. At high current levels, surface impurities and vacuum quality affect the amount of contaminants diffusing into the grains, causing shifts in grain configuration and changes in device operation.	31

LIST OF ILLUSTRATIONS (Continued)

Figure No.		Page
5-2	Schematic diagrams of the hydrogenation process and resulting tip structure. (a) The plasma hydrogen process removes surface oxides and carbons and supplies hydrogen which diffuses into the grain boundaries to stabilize the structure. (b) After hydrogenation the structure is stable at a variety of current levels since all dangling bonds in the grain boundaries near the tip have been passivated. (c) The structure remains stable even at current levels as high as those required to field-form an atomic emitter.	32
6-1	Probability of charge collection by central $24 \times 24\text{-}\mu\text{m}$ pixel illustrated by (a) contour plots and (b) a three-dimensional view. The dashed curve in (a) is the full width at half-maximum.	36
7-1	Multilayer version of Codeman with 2ATC in a standard socket. The circuit uses ten low-power off-the-shelf components for the generation of signals to the 2ATC device.	40
7-2	(a) Photographic and (b) graphic versions of output from Codeman circuit over a complete cycle. This output is input to a 2ATC device under test. The square-wave (SW) and pseudo-noise (PN) code progression is indicated in (b).	41
7-3	(a) Photographic and (b) graphic versions of 2ATC output over a complete cycle resulting from stimulation by Codeman-generated signals. The SW and PN correlation types are indicated in (b).	42
7-4	Comparison of $R_S(H_{rf})$ at 4 K for three YBCO films: a standard off-axis sputtered film, a film deposited with the optimum substrate temperature ($T_{dep} = 760^\circ\text{C}$), and a film deposited by cylindrical magnetron sputtering. Also shown for comparison is the estimated power dependence predicted from Ginzburg-Landau (GL) theory for a thermodynamic critical field $H_c = 1\text{ T}$.	45
7-5	Measurements (squares and dots) and calculations (solid lines) of $b_R(T)$. The solid lines are computed using the critical current density of the Josephson junction weak links in the coupled-grain model as a free parameter to fit the data. The cylindrical magnetron films have a higher weak link critical current density than the standard off-axis films, yielding better power handling.	45

LIST OF ILLUSTRATIONS (Continued)

Figure No.		Page
7-6	Measurements of output power vs input power showing linear response as well as one of two in-band third-order intermodulation products for a four-pole filter fabricated with YBCO film of the same quality as designated standard in Figure 7-4. The solid points are either of the essentially identical output powers of two equal-amplitude closely spaced in-band tones at frequencies f_1 and f_2 , and the open points are the output power at $2f_1-f_2$, with circular and triangular points measured at 4 and 77 K, respectively. Solid lines are drawn to indicate slopes of 1 and 3.	46

LIST OF TABLES

Table No.		Page
1-1	Improvement of Optical Damage with Annealing in Ti-Indiffused LiNbO ₃ Modulators	2
6-1	Collection of Charge Diffusing in Field-Free Region of CCDs	37

INTRODUCTION

1. ELECTROOPTICAL DEVICES

The photorefractive sensitivity of Ti-indiffused optical waveguides in LiNbO_3 has been substantially reduced by using a post-fabrication oxygen anneal. In tests of over 100-h duration with 400 mW at 1320 nm or 80 mW at 1064 nm, these waveguides show no damage other than a small phase shift.

2. QUANTUM ELECTRONICS

Diode-array pumping of 3- μm GaInAsSb/GaSb lasers has yielded 95-mW average and 1.5-W peak power per facet at 85 K. At the same operating temperature, a 4- μm InAsSb/GaSb laser yielded 50-mW average and 0.8-W peak power per facet.

3. MATERIALS RESEARCH

Ridge-waveguide lasers emitting at $\sim 2 \mu\text{m}$ with CW threshold current as low as 29 mA and CW output power as high as 28 mW at room temperature have been fabricated from a GaInAsSb/AlGaAsSb quantum-well heterostructure grown on a GaSb substrate by molecular beam epitaxy. The lasers operate in a single longitudinal mode which can be continuously tuned without mode hopping over 1.2 nm by changing the heatsink temperature and over 0.8 nm by changing the current.

Tapered oscillators emitting at $\sim 2 \mu\text{m}$ have been fabricated from a GaInAsSb/AlGaAsSb quantum-well structure grown by molecular beam epitaxy. These lasers have exhibited CW output power up to 750 mW, with power in the near-diffraction-limited central lobe as high as 200 mW at room temperature.

InAs layers have been grown on GaAs substrates by low-pressure organometallic vapor phase epitaxy over a wide range of substrate temperatures and V/III ratios and have been characterized by electrical, structural, and optical measurements. The best layers were grown at 410°C with a V/III ratio of 15 and had electron mobilities as high as $3.2 \times 10^4 \text{ cm}^2/\text{V s}$ at 77 K and electron carrier concentration of $1.6 \times 10^{16} \text{ cm}^{-3}$.

4. SUBMICROMETER TECHNOLOGY

A model has been developed to predict the behavior of near-surface-imaged resist processes when used for 193-nm lithography. Silylation, bilayer, and additive resist processes can all be simulated with this model.

The resolution, depth of focus, and exposure latitude have been evaluated for 193- and 248-nm photolithography systems. Aerial images were simulated for each system to investigate the effects of numerical aperture, spatial coherence, and annular illumination.

5. HIGH SPEED ELECTRONICS

A qualitative model has been formulated which links the structural properties of polycrystalline molybdenum field-emission cones to emission-current stability and hydrogen-passivation effects. It is shown that observations from the steel industry on molybdenum can explain the improvement in current stability brought about by a hydrogen-plasma treatment.

6. MICROELECTRONICS

The lateral diffusion of charge in the field-free region of a thinned, back-illuminated charge-coupled device (CCD) has been calculated, with the results indicating that the full width at half-maximum of the charge spreading is approximately equal to the dimensions of the CCD pixel. The amount of charge spreading is not a strong function of the initial depth of electrons in the field-free region, so the spreading of electrons generated by photons of different wavelengths is similar.

7. ANALOG DEVICE TECHNOLOGY

A circuit developed for the dual-analog-ternary correlator (2ATC) has been shown to provide all the signals required to demonstrate full functionality of the device in a low-power compact format using off-the-shelf components. The circuit offers test and demonstration capability under conditions where small size, low power requirement, and minimal weight are important.

Measurements of the power dependence of $\text{YBa}_2\text{Cu}_3\text{O}_{7-x}$ thin films deposited by inverted cylindrical magnetron sputtering have shown them to have 50 times higher power-handling capacity than films deposited by other methods. Projections indicate they can be used to fabricate microstrip bandpass filters at 4 GHz able to transmit 50 W with low loss and distortion.

REPORTS ON SOLID STATE RESEARCH

1 MAY THROUGH 31 JULY 1993

PUBLICATIONS

- | | | |
|---|---|--|
| Calculated Room-Temperature Threshold Current Densities for the Visible II-VI ZnCdSe/ZnSe Quantum-Well Diode Lasers | R. L. Aggarwal
J. J. Zayhowski
B. Lax | <i>Appl. Phys. Lett.</i> 62 , 2899 (1993) |
| Designing High Performance KrF and ArF Single Layer Resists with Methacrylate Polymers | R. D. Allen*
G. M. Wallraff*
W. D. Hinsberg*
W. E. Conley*
R. R. Kunz | <i>J. Photopolym. Sci. Technol.</i> 6 , 575 (1993) |
| Externally Modulated Optical Analog Links for Microwave Applications | G. E. Betts | <i>Proceedings of 1993 National Telesystems Conference</i> (IEEE, New York, 1993), p. 13 |
| Frequency Modulation Locking in 980 nm Strained Quantum Well Lasers | S. R. Chinn
C. A. Wang
G. A. Evans* | <i>Electron. Lett.</i> 29 , 646 (1993) |
| Substrate Temperature Measurement for Growth of Large-Area High- T_c Superconducting Films | B. I. Choi*
M. I. Flik*
A. C. Anderson | <i>IEEE Trans. Appl. Superconduct.</i> 3 , 1636 (1993) |
| CW Operation of Monolithic Arrays of Surface-Emitting Folded-Cavity InGaAs/AlGaAs Diode Lasers | J. P. Donnelly
W. D. Goodhue
C. A. Wang
R. J. Bailey
G. A. Lincoln
G. D. Johnson
L. J. Missaggia
J. N. Walpole | <i>IEEE Photon. Technol. Lett.</i> 5 , 747 (1993) |

*Author not at Lincoln Laboratory.

- | | | |
|---|--|---|
| Molecular-Beam Epitaxy Growth of Semiconductor Heterostructure Optical Converter Lasers Using the InGaAs/AlGaAs Materials System | W. D. Goodhue
H. Q. Le
S. DiCecca | } <i>J. Vac. Sci. Technol. B</i> 11 , 948 (1993) |
| Quantum Well GaAs/AlGaAs Shallow-Donor Far-Infrared Photoconductors Grown by Molecular-Beam Epitaxy | W. D. Goodhue
E. R. Mueller*
D. M. Larsen*
J. Waldman*
Y. H. Chai*
S. C. Lai*
G. D. Johnson | |
| Modeling of Positive-Tone Silylation Processes for 193-nm Lithography | M. A. Hartney | <i>J. Vac. Sci. Technol. B</i> 3 , 681 (1993) |
| Experimental Results on a Scanned Beam Microstrip Antenna Array with a Proximity Coupled YBCO Feed Network | J. S. Herd*
D. Hayes*
J. P. Kenney*
L. D. Poles*
K. G. Herd*
W. G. Lyons | <i>IEEE Trans. Appl. Superconduct.</i> 3 , 2840 (1993) |
| Further Developments in Surface Imaging Resists | D. W. Johnson*
R. R. Kunz
M. W. Horn | <i>J. Photopolym. Sci. Technol.</i> 6 , 593 (1993) |
| Octagonal Washer dc SQUIDs and Integrated Susceptometers Fabricated in a Planarized Sub- μm Nb-AlO _x -Nb Technology | M. Ketchen*
D. J. Pearson*
K. Stawiasz*
C.-K. Hu*
A. W. Kleinsasser*
T. Brunner*
C. Cabral*
V. Chandrasekhar*
M. Jaso*
M. Manny*
K. Stein*
M. Bhushan | <i>IEEE Trans. Appl. Superconduct.</i> 3 , 1795 (1993) |

*Author not at Lincoln Laboratory.

Technique for Velocity-Matched
Traveling-Wave Electrooptic
Modulator in AlGaAs/GaAs

M. N. Khan*
A. Gopinath*
J. P. G. Bristow*
J. P. Donnelly

*IEEE Trans. Microwave
Theory Tech.* **41**, 244
(1993)

Resist Processes for ArF Excimer
Laser Lithography

R. R. Kunz
M. A. Hartney
M. W. Horn
C. L. Keast
M. Rothschild
D. C. Shaver

J. Photopolym. Sci. Technol.
6, 473 (1993)

Analysis of Superconducting
Transmission-Line Structures for
Passive Microwave Device
Applications

L. H. Lee*
S. M. Ali*
W. G. Lyons
D. E. Oates
J. D. Goettee*

*IEEE Trans. Appl.
Superconduct.* **3**, 2782
(1993)

Implementation of a $\text{YBa}_2\text{Cu}_3\text{O}_{7-x}$
Wideband Real-Time Spectrum-Analysis
Receiver

W. G. Lyons
D. R. Arsenault
M. M. Seaver
R. R. Boisvert
T. C. L. G. Sollner
R. S. Withers

*IEEE Trans. Appl.
Superconduct.* **3**, 2891
(1993)

Nonlinear Surface Resistance in
 $\text{YBa}_2\text{Cu}_3\text{O}_{7-x}$ Thin Films

D. E. Oates
P. P. Nguyen*
G. Dresselhaus*
M. S. Dresselhaus*
C. C. Chin*

*IEEE Trans. Appl.
Superconduct.* **3**, 1114
(1993)

A Nonlinear Transmission Line
Model for Superconducting Stripline
Resonators

J. H. Oates*
R. T. Shin*
D. E. Oates
M. J. Tsuk*
P. P. Nguyen*

*IEEE Trans. Appl.
Superconduct.* **3**, 17
(1993)

*Author not at Lincoln Laboratory.

- | | | |
|--|---|---|
| Electrical Properties of MBE Grown Layers of AlGaAsSb and the Effects of Proton Implantation and Hydrogen Plasma Treatment | A. Y. Polyakov*
S. J. Eglash
A. G. Milnes*
M. Ye*
S. J. Pearton*
R. G. Wilson* | <i>J. Cryst. Growth</i> 127 , 728 (1993) |
| Integrated Electronic Shutter for Back-Illuminated Charge-Coupled Devices | R. K. Reich
R. W. Mountain
W. H. McGonagle
J. C. M. Huang
J. C. Twichell
B. B. Kosicki
E. D. Savoye | <i>IEEE Trans. Electron Devices</i> 40 , 1231 (1993) |
| Excimer Laser Induced Degradation in Bulk Fused Silica | M. Rothschild
J. H. C. Sedlacek | <i>Proc. SPIE</i> 1848 , 537 (1993) |
| Design, Fabrication, and Testing of a High-Speed Analog Sampler | J. P. Sage
J. B. Green
A. Davidson* | <i>IEEE Trans. Appl. Superconduct.</i> 3 , 2562 (1993) |
| Femtosecond Gain Dynamics in InGaAs/AlGaAs Strained-Layer Single-Quantum-Well Diode Lasers | C.-K. Sun*
H. K. Choi
C. A. Wang
J. G. Fujimoto* | <i>Appl. Phys. Lett.</i> 63 , 96 (1993) |
| Molecular-Beam Epitaxial Growth of High-Mobility <i>n</i> -GaAs | G. W. Turner
S. J. Eglash
A. J. Strauss | <i>J. Vac. Sci. Technol. B</i> 11 , 864 (1993) |
| Vortex Dynamics in One-Dimensional Parallel Arrays of Underdamped Josephson Junctions | H. S. J. van der Zant*
E. H. Visscher*
D. R. Curd*
T. P. Orlando*
K. A. Delin | <i>IEEE Trans. Appl. Superconduct.</i> 3 , 2658 (1993) |

*Author not at Lincoln Laboratory.

ACCEPTED FOR PUBLICATION

The Monolithic Optoelectronic
Transistor: A New Smart
Pixel Device

B. F. Aull
K. B. Nichols
P. A. Maki
S. C. Palmateer
E. R. Brown
T. A. Lind

Appl. Phys. Lett.

Solid-State Lasers

T. Y. Fan

In *Encyclopedia of
Applied Physics* (VCH
Publishers, New York)

High Conductance, Low Leakage
Diamond Schottky Diodes

M. W. Geis
N. N. Efremow
J. A. von Windheim*

Appl. Phys. Lett.

Experiment and Simulation of
Sub-0.25- μm Resist Processes for
193-nm Lithography

R. R. Kunz
M. A. Hartney
R. W. Otten, Jr.*

Proc. SPIE

Design of Acid-Catalyzed Single-Layer
Resists for ArF Lithography

R. R. Kunz
G. M. Wallraff*
R. D. Allen*
W. D. Hinsberg*

Proc. SPIE

4-W Average Power, Low Internal
Loss, Diode Laser Pumped InGaAs/
GaAs/AlGaAs Heterostructure Lasers

H. Q. Le
W. D. Goodhue
P. A. Maki
S. DiCecca

Appl. Phys. Lett.

Three-Wavelength Interconversion Laser

P. A. Schulz
T. H. Jeys

Opt. Lett.

$\text{Ge}_x\text{Si}_{1-x}$ -Si Heterojunction Infrared
Detectors and Focal Plane Arrays

B-Y. Tsaur
C. K. Chen
S. A. Marino

Opt. Eng.

*Author not at Lincoln Laboratory.

The Effect of Back Contact Impedance
on Frequency Dependence of
Capacitance-Voltage Measurements
on Metal/Diamond Diodes

V. Venkatesan*
K. Das*
J. A. von Windheim*
M. W. Geis

Appl. Phys. Lett.

A Ti:Al₂O₃ Master-Oscillator/Power-
Amplifier System

K. F. Wall
P. A. Schulz
R. L. Aggarwal
P. Lacovara
A. Sanchez

IEEE J. Quantum Electron.

Critical Layer Thickness of Strained-
Layer InGaAs/GaAs Multiple Quantum
Wells Determined by Double-Crystal
X-Ray Diffraction

C. A. Wang
S. H. Groves
J. H. Reinold
D. R. Calawa

J. Electron. Mater.

Adjusting Trimethylgallium Injection
Time to Obtain Atomic Layer Epitaxy
of GaAs Between 425 and 500°C by
Organometallic Vapor Phase Epitaxy

C. A. Wang
D. M. Tracy

J. Electron. Mater.

Diode-Pumped Composite-Cavity
Electrooptically Tuned Microchip
Laser

J. J. Zayhowski
P. A. Schulz
C. Dill III
S. R. Henion

IEEE Photon. Technol. Lett.

PRESENTATIONS[†]

The Monolithic Optoelectronic
Transistor

B. F. Aull
K. B. Nichols
P. A. Maki
S. C. Palmateer
E. R. Brown
T. A. Lind

1993 Conference on Lasers
and Electro-Optics,
Baltimore, Maryland,
2-7 May 1993

*Author not at Lincoln Laboratory.

[†]Titles of presentations are listed for information only. No copies are available for distribution.

Aperture Guiding in CW, Quasi-Three-Level Yb:YAG Lasers

T. Y. Fan
P. A. Schulz

Holmium Laser Pumped by 1.9- μ m Diode Laser

C. D. Nabors
T. Y. Fan
H. K. Choi
G. W. Turner
S. J. Eglash

Femtosecond Carrier Dynamics and Stimulated Transitions Induced Carrier Temperature Change in InGaAs/AlGaAs Strained-Layer SQW Diode Lasers

C.-K. Sun*
H. K. Choi
C. A. Wang
J. G. Fujimoto*

Diode-Pumped Composite-Cavity Electro-optically Tuned Microchip Laser

J. J. Zayhowski
P. A. Schulz
S. R. Henion

Multiple-Quantum-Well Optoelectronic Devices

B. F. Aull

Application of Frequency-Domain Analysis to RHEED Oscillation Data: Time Dependence of AlGaAs Growth Rates

G. W. Turner
S. J. Eglash

High-Power GaInAsSb/AlGaAsSb Quantum-Well Diode Lasers

H. K. Choi
G. W. Turner
J. N. Walpole
S. J. Eglash

Diamond Review

M. W. Geis
J. C. Twichell

1993 Conference on Lasers and Electro-Optics,
Baltimore, Maryland,
2-7 May 1993

Lincoln Laboratory
Technical Seminar Series,
University of Wisconsin,
Madison, Wisconsin,
3 May 1993

Lincoln Laboratory
Technical Seminar Series,
Georgia Institute of
Technology,
Atlanta, Georgia,
5 May 1993

1993 Semiconductor Laser
Workshop,
Baltimore, Maryland,
7 May 1993

Seminar, AT&T Bell
Laboratories,
Murray Hill, New Jersey,
11 May 1993

*Author not at Lincoln Laboratory.

An Ionic Liquid-Channel Field-Effect Transistor

**S. A. Gajar
M. W. Geis**

Photolithography and Resist Technology at 193 nm for 0.25 μm and Beyond

**M. W. Horn
R. B. Goodman
M. A. Hartney
C. L. Keast
R. R. Kunz
M. Rothschild
J. H. C. Sedlacek
D. C. Shaver**

**183rd Meeting of the
Electrochemical Society,
Honolulu, Hawaii,
16-21 May 1993**

Low Temperature Etching of Silylated Resist in an Oxygen Plasma Generated by an Electron Cyclotron Resonance Source

**K. T. Sung*
W. H. Juan*
S. W. Pang*
M. W. Horn**

Superconductor Electronic Devices and System Applications

W. G. Lyons

**IEEE Electron Devices Society,
Boston Chapter Meeting,
Waltham, Massachusetts,
20 May 1993**

Optoelectronic Techniques for Phased-Array Signal Distribution and Processing

L. M. Johnson

**IEEE Aerospace and Electronic
Systems Seminar,
Sudbury, Massachusetts,
27 May 1993**

Design of Acid-Catalyzed Single-Layer Resists for ArF Lithography

**R. R. Kunz
G. M. Wallraff*
R. D. Allen*
W. D. Hinsberg***

**37th International Symposium
on Electron, Ion, and Photon
Beams,
San Diego, California,
1-4 June 1993**

Evaluation of Depth of Focus in Photolithography at 0.25 μm and Below

**M. Rothschild
E. Barouch*
U. Hollerbach*
S. Orszag***

***Author not at Lincoln Laboratory.**

**Resist Processes for ArF Excimer Laser
Lithography**

R. R. Kunz
M. A. Hartney
M. W. Horn
M. Rothschild
D. C. Shaver
C. L. Keast

Seminar, AT&T Bell Laboratories,
Murray Hill, New Jersey,
14 June 1993

**Full-Wave Analysis of Superconducting
Microstrip Lines on Sapphire Substrates**

L. H. Lee*
S. M. Ali*
W. G. Lyons
R. W. Withers*
T. P. Orlando*

1993 IEEE MTT-S International
Microwave Symposium,
Atlanta, Georgia,
14-18 June 1993

Photolithography at 193 nm

M. Rothschild

Seminars, Intel and
Advanced Micro Devices,
Palo Alto, California,
17 June 1993

**A Vertical Schottky-Gated Resonant
Tunneling Transistor with High
Transconductance at Room
Temperature**

W. C. B. Peatman*
E. R. Brown
M. J. Rooks*
P. A. Maki
M. Shur*

51st Annual Device Research
Conference,
Santa Barbara, California,
21 June 1993

**Arrays of Gated Field-Emitter Cones
Having 0.32- μ m Tip-to-Tip Spacings**

C. O. Bozler
C. T. Harris
S. Rabe
D. D. Rathman
W. D. Goodhue
M. A. Hollis
H. I. Smith*

Sixth International Vacuum
Microelectronics Conference,
Newport, Rhode Island,
12-15 July 1993

*Author not at Lincoln Laboratory.

**Bright-Field Analysis of Field-Emission
Cones Using High-Resolution
Transmission Electron Microscopy**

W. D. Goodhue
P. M. Nitishin
C. T. Harris
C. O. Bozler
D. D. Rathman
G. D. Johnson
M. A. Hollis

Sixth International Vacuum
Microelectronics Conference,
Newport, Rhode Island,
12-15 July 1993

**The Effect of Space Charge on Vacuum
Microtriode RF Performance**

D. D. Rathman
M. A. Hollis
R. A. Murphy

**The Monolithic Optoelectronic
Transistor: A New Optical
Neuron Device**

B. F. Aull
E. R. Brown
P. A. Maki
K. B. Nichols
S. C. Palmateer
T. A. Lind

SPIE's Conference on
Optoelectronic Neural
Networks,
San Diego, California,
14 July 1993

**20-Channel Optoelectronic Receiver for
Free-Space Optical Interconnection**

K. D. Pedrotti*
C. W. Seabury*
R. L. Pierson*
D. Z. Tsang

IEEE Lasers and Electro-Optics
Society Summer Topical
Meetings,
Santa Barbara, California,
26-28 July 1993

*Author not at Lincoln Laboratory.

ORGANIZATION

SOLID STATE DIVISION

A. L. McWhorter, *Head*
I. Melngailis, *Associate Head*
E. Stern, *Associate Head*
D. C. Shaver, *Assistant Head*
J. F. Goodwin, *Assistant*

D. J. Ehrlich, *Senior Staff*
N. I. DeMeo, Jr., *Associate Staff*
J. W. Caunt, *Assistant Staff*
K. J. Challberg, *Administrative Staff*

SUBMICROMETER TECHNOLOGY

M. Rothschild, *Leader*
T. M. Lyszczarz, *Assistant Leader*

Astolfi, D. K.	Horn, M. W.
Craig, D. M.	Keast, C. L.
Dennis, C. L.	Kunz, R. R.
DiNatale, W. F.	Maki, P. A.
Doran, S. P.	Melngailis, J. [†]
Efremow, N. N., Jr.	Palmateer, S. C.
Forte, A. R.	Sedlacek, J. H. C.
Geis, M. W.	Twitchell, J. C.
Goodman, R. B.	Uttaro, R. S.
Hartney, M. A.	

QUANTUM ELECTRONICS

A. Sanchez-Rubio, *Leader*
T. Y. Fan, *Assistant Leader*

Aggarwal, R. L.	Hsu, L.*
Cook, C. C.	Jeys, T. H.
Daneu, V.	Kelley, P. L. [‡]
DeFeo, W. E.	Le, H. Q.
DiCecca, S.	Nabors, C. D.
Dill, C. D., III	Ochoa, J. R.
Hotaling, T. C.	Zayhowski, J. J.

ELECTRONIC MATERIALS

B-Y. Tsaur, *Leader*
D. L. Spears, *Assistant Leader*

Anderson, C. H., Jr.	Krohn, L., Jr.
Button, M. J.	Marino, S. A.
Chen, C. K.	McGilvary, W. L.
Choi, H. K.	Nitishin, P. M.
Connors, M. K.	Pantano, J. V.
Fahey, R. E.	Reinold, J. H., Jr.
Finn, M. C.	Turner, G. W.
Harman, T. C.	Wang, C. A.
Iseler, G. W.	

HIGH SPEED ELECTRONICS

R. A. Murphy, *Leader*
M. A. Hollis, *Assistant Leader*

Bozler, C. O.	Mathews, R. H.
Brown, E. R.	Mattia, J. P.*
Chen, C. L.	McIntosh, K. A.
Clifton, B. J. [‡]	Nichols, K. B.
Goodhue, W. D.	Parker, C. D.
Harris, C. T.	Rabe, S.
Lincoln, G. A., Jr.	Rathman, D. D.
Mahoney, L. J.	Smith, F. W., III
Manfra, M. J.	

* Research Assistant

[†] Part Time

[‡] Leave of Absence

ELECTROOPTICAL DEVICES

R. C. Williamson, *Leader*
L. M. Johnson, *Assistant Leader*

Aull, B. F.	Missaggia, L. J.
Bailey, R. J.	Mull, D. E.
Betts, G. E.	O'Donnell, F. J.
Donnelly, J. P.	Palmacci, S. T.
Golubovic, B.*	Reeder, R. E.
Groves, S. H.	Roussell, H. V.
Hovey, D. L.	Tsang, D. Z.
Liau, Z. L.	Walpole, J. N.
Lind, T. A.	Woodhouse, J. D.

ANALOG DEVICE TECHNOLOGY

R. W. Ralston, *Leader*
T. C. L. G. Sollner, *Assistant Leader*
P. M. Mankiewich, *Assistant Leader*
A. C. Anderson, *Senior Staff*
A. M. Chiang, *Senior Staff*

Abusch, D. M.*	LaFranchise, J. R.
Arsenault, D. R.	Linden, D. S.*
Boisvert, R. R.	Lyons, W. G.
Brogan, W. T.	Macedo, E. M., Jr.
Delin, K. A.	Oates, D. E.
Denneno, J. M.	Sage, J. P.
Fitch, G. L.	Seaver, M. M.
Green, J. B.†	Slattery, R. L.
Holtham, J. H.	Tam, K.*

MICROELECTRONICS

E. D. Savoye, *Leader*
B. B. Kosicki, *Assistant Leader*
B. E. Burke, *Senior Staff*

Clark, H. R., Jr.	Felton, B. J.	Mountain, R. W.
Daniels, P. J.	Gregory, J. A.	Percival, K. A.
Doherty, C. L., Jr.	Johnson, K. F.	Pichler, H. H.
Dolat, V. S.	Loomis, A. H.	Reich, R. K.
Donahue, T. C.	McGonagle, W. H.	Young, D. J.

* Research Assistant

† Leave of Absence

1. ELECTROOPTICAL DEVICES

1.1 EFFECT OF ANNEALING ON PHOTOREFRACTIVE DAMAGE IN Ti-INDIFFUSED LiNbO₃ MODULATORS

The photorefractive sensitivity of Ti:LiNbO₃ interferometric modulators has been shown [1],[2] to be affected by device annealing, with increased sensitivity demonstrated at annealing temperatures as low as 200°C in nonoxygen atmospheres. Conversely, this report describes how photorefractive sensitivity can be significantly reduced by anneals in an oxygen atmosphere.

The basic optical damage mechanism is the photorefractive effect, in which illuminated regions experience a refractive index change. This effect, which is caused by photoionization of the Fe²⁺ impurity, results in many different phenomena in waveguides, which in turn cause changes in modulator performance. The measurements reported here were all made on Mach-Zehnder interferometric modulators fabricated on X-cut, Y-propagating substrates with Ti-indiffused waveguides. The most sensitive measure of damage in these devices is usually a change in the phase bias, defined as the quiescent optical phase difference between the arms. Different index changes in the two arms cause changes in the phase bias. The extinction, which is the ratio of maximum to minimum optical transmission [1], can be degraded by unbalanced losses in the arms and/or by unbalanced splitting at the Y-branches. The optical transmission can be reduced by increased waveguide losses. Ionized electrons can move to cancel applied dc fields, which is referred to as the photoconductive effect.

In our measurements, the modulator phase bias was determined by applying a 1-kHz sine wave to the electrodes and measuring the first and second harmonic output signals. In a typical test, the device was aligned and data recording begun using an input optical power of ~ 1 mW. (All of the measurements reported here at this power level showed a stable phase bias, except for the first measurement in Table 1-1, which indicated a small drift.) The optical power was then increased to the measurement level and held approximately constant. No dc voltage was applied except during photoconductive measurements. The changes in phase bias reported here are all relative to the bias immediately prior to the time the optical power was increased for each separate measurement.

Table 1-1 summarizes a series of measurements showing the change in photorefractive sensitivity of a single device following sequential anneals. The measurements were performed at 1064-nm wavelength with times of 115–160 h and power levels of 60–90 mW, which correspond to spatial peak intensities of 0.70–1.0 MW/cm². The variation in power levels and times used in the different tests in Table 1-1 was small enough that it caused only small differences in photorefractive effects compared to the magnitude of the effects observed. For a device fabricated with a single 7-h, 500°C anneal in wet oxygen, the extinction degraded to a minimum of 14 dB and then partially recovered, the phase bias drifted about 500°, and the optical transmission dropped by up to 1 dB. A second anneal in wet oxygen reduced the sensitivity to the point where no photorefractive effects were observed except for a 23° drift in the modulator phase bias. The extinction of 17 dB is lower than the 20 dB typical for these devices, but it did not vary with time or optical power level, indicating no changes in extinction due to photorefractive effects. A third anneal in wet oxygen did not alter the performance. Finally, a 16-h, 120°C anneal in dry nitrogen not only did not diminish but actually enhanced the improvement in optical power handling ability gained by these wet oxygen anneals.

TABLE 1-1

Improvement of Optical Damage with Annealing in Ti-Indiffused LiNbO₃ Modulators*

Device No.	Anneal			Photorefractive Effects	
	Time (h)	Temperature (°C)	Gas	Bias Drift (deg)	Minimum Extinction (dB)
2	7	500	Wet O ₂	500	14
2	7	500	Wet O ₂	23	17
2	7	500	Wet O ₂	28	17
2	16	120	Dry N ₂	3	23

*Damage test: 1064 nm, 60–90 mW, 115–160 h.

Long-term power-handling measurements are shown in Figure 1-1 for a set of devices fabricated using two 7-h, 500°C anneals in wet oxygen. At 1320 nm, there was no measurable change in phase bias at 100 mW and only 3.5° drift over 150 h at 400 mW. The waveguides in the 1320-nm devices had elliptical modes with $1/e^2$ -intensity dimensions of $\sim 7.5 \mu\text{m}$ (along Z) $\times 5.0 \mu\text{m}$ (along X), which resulted in a spatial peak intensity of $\sim 3 \text{ MW/cm}^2$ in the 400-mW measurement. At 1064 nm, the phase bias drift was 28° over 160 h at 90 mW. No photorefractive effects were observed in these tests other than the phase bias drifts. This performance equals or exceeds the performance of devices we have fabricated using annealed proton exchange in LiNbO₃.

In photoconductive tests of several wet-oxygen-annealed devices, a dc voltage was first applied that was several times larger than the switching voltage V_π of the modulator. The optical power was then increased and the measurement started, during which the modulator phase bias was held at a fixed value by using an electrical control circuit to vary the applied dc voltage. The measured quantity was the value of the applied dc voltage. The result of a photoconductive test at 1064 nm is shown in Figure 1-2. The voltage remained reasonably steady with variation $< 0.5V_\pi$, and no other photorefractive effects were observed, showing that the photoconductive effect does not interfere with active dc bias control. (This does not imply that there is no photoconductive effect, but only that the effect is small or that there is current flow in the external circuit [3].)

A possible explanation for the results obtained here is that the last high-temperature anneal process that the device experiences before it is optically tested affects the $\text{Fe}^{2+}:\text{Fe}^{3+}$ ratio, with wet oxygen anneals decreasing the ratio [4]. In addition, water vapor is expected to play a role in damage reduction [5], although this effect was reported at processing temperatures $\geq 600^\circ\text{C}$. Positively charged ions can move to compensate the fields produced by the photorefractive effect at 100–150°C [6], and in the “thermal fixing” method for reducing photorefractive sensitivity [7] this provides an advantage. The ionic mobility effect did not seem to be a factor in our measurements, because most of our anneals were done either at temperatures $> 200^\circ\text{C}$ where electronic conduction dominates or on samples with no prior optical damage, or both. The one exception was the dry nitrogen anneal at 120°C, shown in Table 1-1, where

the reduced bias drift may be explained by thermal fixing. However, because thermal fixing depends upon ions that are mobile at temperatures of 125°C or less, this performance improvement may not be reliable in practical applications. The primary conclusion from this measurement is that storage at 125°C in dry nitrogen does not return the device to a state of high damage sensitivity.

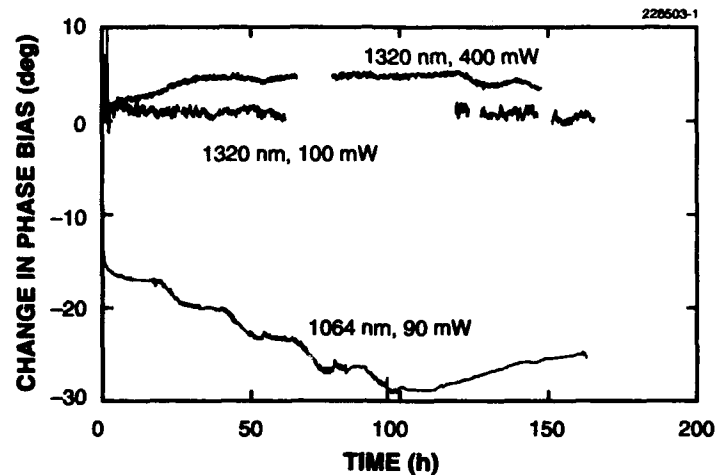


Figure 1-1. Phase bias drift in modulators annealed twice for 7 h at 500°C in wet oxygen. No photorefractive-related decrease in optical transmission occurred during these tests. (Gaps in the data are due to recording failures; the optical power remained on.)

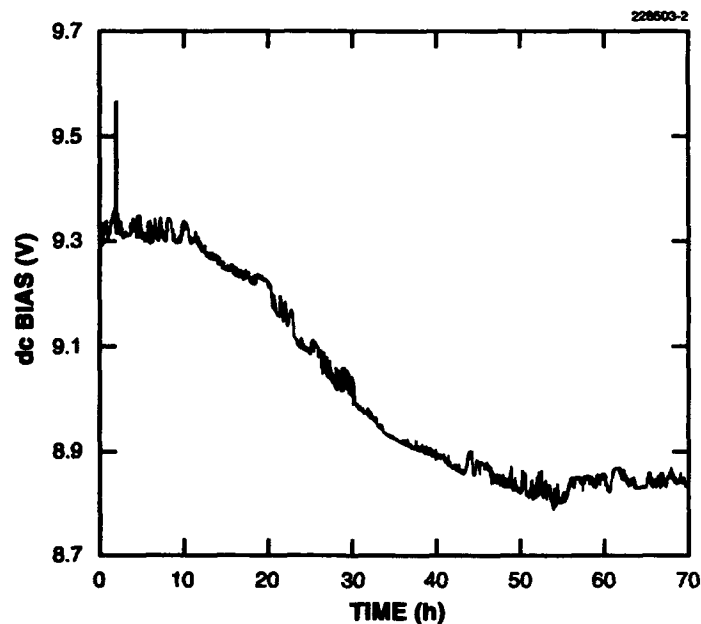


Figure 1-2. Result of photoconductive test with 90 mW at 1064 nm. The dc bias voltage was controlled to maintain a constant modulator phase bias. The V_x was 1.1 V for this device.

The photorefractive sensitivity of these Ti-indiffused modulators, when they are annealed adequately in wet oxygen, is low enough for most practical applications. At 1320 nm, there are no optical transmission or extinction ratio problems even at 400 mW. The phase bias drift is small enough that the devices do not require active bias control at power levels up to 100 mW. At 1064 nm, at power levels up to 90 mW, the phase bias drift is large enough that an active bias control circuit would be required in most applications. Other photorefractive effects, however, are very small. The photorefractive sensitivity does not degrade when the devices are annealed 16 h at 120°C in dry nitrogen, so this performance should be reliable even in applications that require devices in hermetic packages to withstand 125°C.

G. E. Betts
F. J. O'Donnell
K. G. Ray

REFERENCES

1. Solid State Research Report, Lincoln Laboratory, MIT, 1992:3, p. 5.
2. G. E. Betts, F. J. O'Donnell, and K. G. Ray, to be published.
3. M. M. Howerton and W. K. Burns, *J. Lightwave Technol.* **10**, 142 (1992).
4. A. M. Glass, *Opt. Eng.* **17**, 470 (1978).
5. R. G. Smith, D. B. Fraser, R. T. Denton, and T. C. Rich, *J. Appl. Phys.* **39**, 4600 (1968).
6. M. G. Clark, F. J. DiSalvo, A. M. Glass, and G. E. Peterson, *J. Chem. Phys.* **59**, 6209 (1973).
7. R. A. Becker, *Appl. Phys. Lett.* **45**, 121 (1984).

2. QUANTUM ELECTRONICS

2.1 HIGH-POWER GaSb-BASED LASERS EMITTING AT 3-4 μm

GaSb-based semiconductor alloys are a promising materials system for developing 2-5 μm laser sources. Room-temperature high-power diode lasers have been demonstrated at 2 μm [1]. For 3 μm and longer, the problem is more challenging, because low-temperature operation is required which causes difficult electrical injection problems. For these GaSb-based materials and some II-VI semiconductors with similar drawbacks, optical pumping is a useful alternative with advantageous aspects such as low internal loss, large optical modes, and flexible power-scaling geometry [2]. By using high-power GaAs diode arrays as pump sources, we have demonstrated GaSb-based broad-stripe lasers emitting from 3 to 4 μm with peak or average power approximately 2 orders of magnitude higher than the best previously reported results for both III-V and II-VI semiconductor lasers.

The laser heterostructures are grown by molecular beam epitaxy and consist of a 0.7-1- μm -thick InAsSb or metastable GaInAsSb active layer, sandwiched between two 2-3- μm -thick AlGaAsSb or AlGaSb cladding layers. The bandgaps of the AlGaAsSb or AlGaSb claddings are higher than the pumping photon energy of 1.5 or 1.39 eV, so that carriers are optically generated and confined within the active layer.

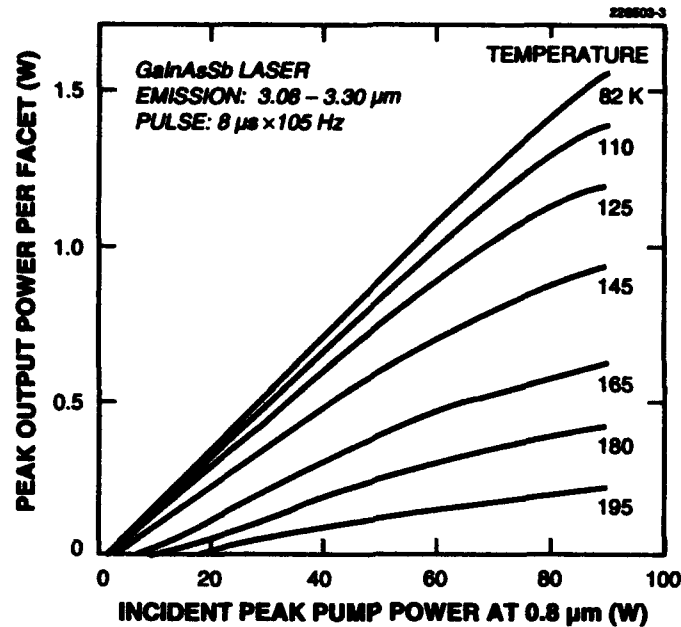
The power output of the 3- μm GaInAsSb and 4- μm InAsSb lasers is shown in Figures 2-1 and 2-2, respectively. The pulse length was 8 μs , and the repetition rate was varied up to 15 kHz. The pulse peak output power at low duty cycle for various temperatures is shown in Figures 2-1(a) and 2-2(a), and the peak and maximum average output power at approximately fixed temperature for increasing duty cycle is shown in Figures 2-1(b) and 2-2(b). The emission wavelength increased from 3.08 to 3.30 μm for the GaInAsSb laser as the temperature increased from 82 to 195 K, and from 3.86 to 3.97 μm for the InAsSb laser as the temperature increased from 80 to 148 K. Lasing operation was observed up to 210 K, which is not shown in Figure 2-1(a) because the power output was very low.

These laser structures, not tailored specifically for optical pumping, exhibit low external quantum efficiency, probably because of high free-carrier absorption loss associated with high doping levels. Structures that are undoped and optimized for optical pumping are likely to have higher efficiency and also to offer more flexibility for use in techniques to obtain high beam quality.

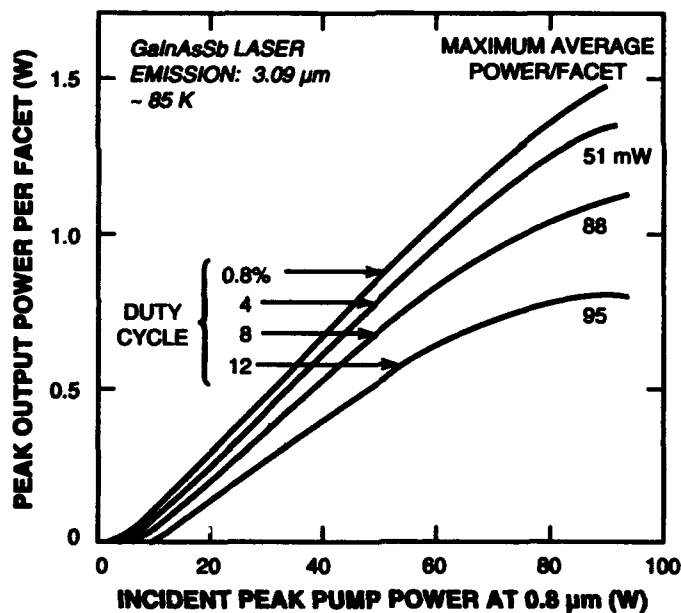
H. Q. Le	S. J. Eglash
G. W. Turner	H. K. Choi

REFERENCES

1. S. J. Eglash, H. K. Choi, G. W. Turner, and M. C. Finn, *Mater. Res. Soc. Symp. Proc.* **216**, 207 (1991).
2. H. Q. Le, W. D. Goodhue, P. A. Maki, and S. DiCecca, *Appl. Phys. Lett.* **63**, 1465 (1993).



(a)



(b)

Figure 2-1. Power output of GaInAsSb/GaSb laser pumped with 0.8- μm diode array: (a) peak power at 0.08% duty cycle for various temperatures, and (b) peak and maximum average power for various duty cycles at 85 K.

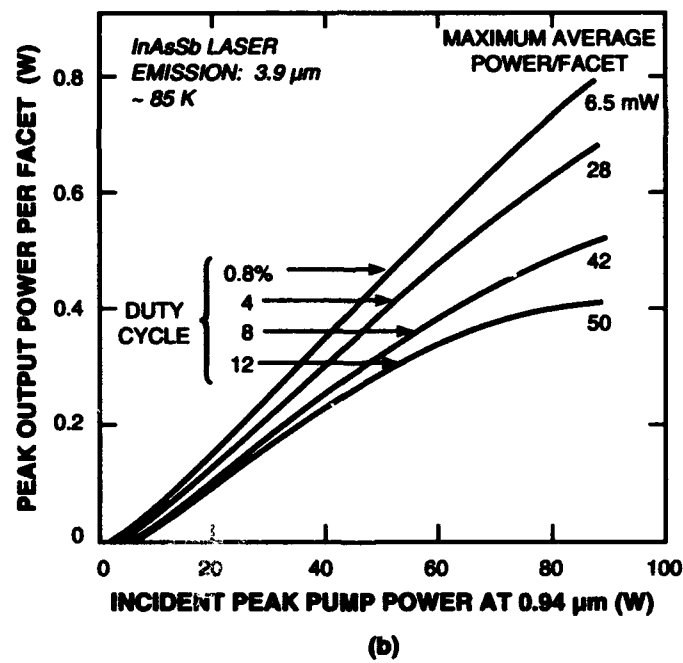
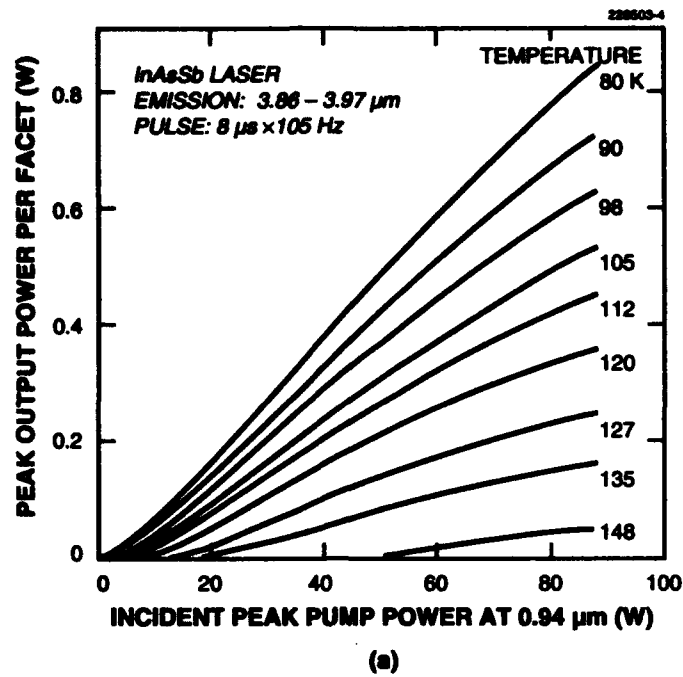


Figure 2-2. Power output of InAsSb/GaSb laser pumped with 0.94- μm diode array: (a) peak power at 0.08% duty cycle for various temperatures, and (b) peak and maximum average power for various duty cycles at 85 K.

3. MATERIALS RESEARCH

3.1 SINGLE-FREQUENCY GaInAsSb/AlGaAsSb QUANTUM-WELL RIDGE-WAVEGUIDE LASERS EMITTING AT 2.1 μm

Single-frequency diode lasers emitting between 2 and 5 μm are strongly needed for spectroscopy, molecular sensing, and pollution monitoring. The absorption strength of many molecules is much greater in this wavelength band than in the near infrared where high-performance diode lasers are available. Diode lasers consisting of a GaInAsSb active region and AlGaAsSb cladding layers have been developed for 2–5- μm sources. Recently, significant improvements in room-temperature performance of 2- μm diode lasers have been achieved by employing a GaInAsSb/AlGaAsSb quantum-well active region and AlGaAsSb cladding layers [1],[2]. Broad-stripe lasers have exhibited pulsed threshold current density as low as 260 A/cm², differential quantum efficiency as high as 70%, and single-ended CW output power as high as 600 mW. The broad-stripe lasers, however, emit in multiple frequencies (longitudinal modes) with separation between modes inversely proportional to the cavity length. Ridge-waveguide lasers fabricated in a GaInAsSb/AlGaAsSb double heterostructure were reported previously [3]. Threshold currents as low as 80 mA were obtained, but the emission spectrum showed multiple longitudinal modes. Here, we report the single-frequency operation of ridge-waveguide lasers fabricated in a GaInAsSb/AlGaAsSb quantum-well heterostructure.

To prepare a wafer for laser fabrication, the following layers were grown on an n -GaSb substrate by molecular beam epitaxy: n^+ -GaSb buffer, n -AlGaAsSb cladding, active region consisting of five unintentionally doped 10-nm-thick GaInAsSb wells and six 20-nm-thick AlGaAsSb barriers, p -AlGaAsSb cladding, and p^+ -GaSb contacting. All the layers are nominally lattice matched to the substrate, except for the quantum wells, which are under compressive strain. The compressive strain has been found to reduce the threshold current density substantially.

Figure 3-1 shows the schematic of the ridge-waveguide laser. The ridges $\sim 8 \mu\text{m}$ wide were formed by reactive ion etching in a BCl_3/Ar plasma. Because the GaSb and AlGaAsSb layers are etched at equal rates by this technique, it was relatively easy to control the etch depth, which was crucial for obtaining a single-mode waveguide.

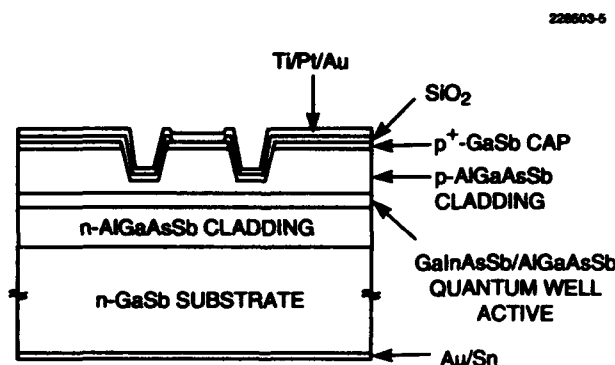


Figure 3-1. Schematic of ridge-waveguide laser. The width of the ridge is 8 μm .

For uncoated devices with cavity length $L = 300, 500,$ and $1000 \mu\text{m}$, the CW threshold currents were 29, 45, and 70 mA, respectively. One device with $L = 300 \mu\text{m}$ has CW output power up to 12.5 mW/facet with an initial slope efficiency of 0.1 W/A per facet, corresponding to a differential quantum efficiency of 17.5%/facet. Devices with $L = 1000 \mu\text{m}$ were coated for high reflection ($> 95\%$) on the back facet and for partial antireflection ($\sim 3\%$) on the front facet. Figure 3-2 shows the CW output power vs current for a coated device at a heatsink temperature of 20°C . The threshold current is 75 mA and differential quantum efficiency 23%. The maximum output power is 28 mW. The lateral far-field pattern shows a single fundamental mode up to the maximum output power with a full width at half-maximum (FWHM) of $\sim 20^\circ$. There is no change in the peak position or the width of the pattern. The FWHM of the transverse far field is $\sim 50^\circ$.

Figure 3-3 shows the emission spectrum of the same device at 130 mA CW at a heatsink temperature of 18°C . It has a single longitudinal mode at $\sim 2.135 \mu\text{m}$ with a side-mode suppression ratio of at least 20 dB. As the current is increased to 180 mA, the single-mode operation is maintained and the mode shifts to longer wavelengths without mode hopping at a rate of 0.016 nm/mA. At higher currents the spectrum shows multiple longitudinal modes, even though the far-field pattern continues to display the fundamental spatial mode. For GaAs/AlGaAs lasers, index guiding along the junction plane is usually sufficient to obtain single-longitudinal-mode operation. The mechanism for single-mode operation in index-guided lasers has been explained by the homogeneously broadened gain and by a smaller spontaneous emission factor than for gain-guided lasers [4]. On the other hand, index-guided GaInAsP/InP lasers without distributed feedback or distributed Bragg reflectors exhibit multiple longitudinal modes. To our best knowledge, the fact that these lasers do not operate in a single longitudinal mode has not been explained.

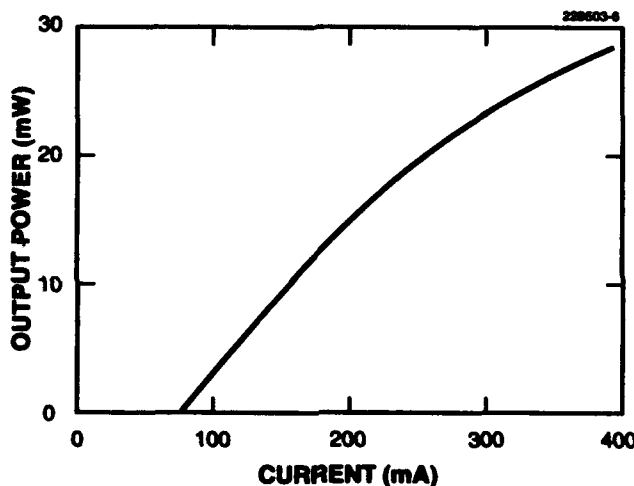


Figure 3-2. Light output vs current for GaInAsSb/AlGaAsSb ridge-waveguide laser under CW operation. The cavity length is $1000 \mu\text{m}$ and reflectivities for back and front facets are 95 and 3%, respectively.

3.3 GROWTH OF InAs ON GaAs SUBSTRATES BY ORGANOMETALLIC VAPOR PHASE EPITAXY

The III-V semiconductor InAs, which has a direct bandgap of 0.36 eV at room temperature, is an important material for infrared detectors and sources. There are only a few reports on epitaxial growth of InAs by organometallic vapor phase epitaxy (OMVPE) at atmospheric pressure [11]–[13], and no reports on growth at low pressure. We present results of a study of InAs grown on GaAs substrates by low-pressure OMVPE. To establish the best growth parameters, the electrical, structural, and optical qualities of the InAs epilayers were evaluated for a range of growth temperatures and V/III ratios.

The InAs epilayers were grown in a vertical rotating-disk (250 rpm) OMVPE reactor operated at 0.2 atm. The source materials were trimethylindium (TMIn), trimethylgallium, and 100% arsine. The carrier gas was H_2 at a flow rate of 10 slpm. The TMIn mole fraction was 1×10^{-4} and the arsine mole fraction ranged from 7.5×10^{-4} to 2×10^{-2} , which resulted in a nominal V/III ratio range between 7.5 and 200. The InAs growth temperature was varied from 350 to 540°C. Since semi-insulating InAs substrates are not available, for ease of electrical characterization, InAs epilayers were grown on semi-insulating (001) GaAs substrates oriented 2° toward [110]. First, a 40-nm-thick GaAs buffer layer was grown at 680°C. The wafer was then cooled under an arsine flow to the growth temperature used for InAs.

The surface morphology of the InAs layers was examined by Nomarski contrast microscopy. The layer thickness was measured by Dektak profiling a sample that had been partially masked and selectively etched down to the GaAs buffer layer with concentrated HCl. Structural characterization was performed by double-crystal x-ray diffraction (DCXRD), electrical characterization by Hall measurements, and optical characterization by photoluminescence (PL) at 4.5 K.

The surface morphology of InAs layers grown at temperatures of 425°C and below was mirror to the eye and showed a slight texture under Nomarski microscopy. Whisker-like defects, which were found by Auger analysis to be stoichiometric InAs, were observed only for layers grown with V/III ratio greater than ~ 20. For epilayers grown at temperatures of 450°C and above and with V/III ratio in the range 15–200, a poor surface morphology which was hazy to the eye was always observed.

The effect of temperature on InAs growth rate is shown in Figure 3-7 for a V/III of either 15 or 25. InAs growth is mass transport limited for the temperature range 410–500°C, and kinetically controlled below 410°C and above 500°C. The activation energy for growth in the lower-temperature kinetic regime is 23.5 kcal/mol, which is nearly the same value (24 kcal/mol) obtained by Ma et al. [13] for InAs growth from TMIn and arsine at atmospheric pressure. In the higher temperature range of kinetically controlled growth, the activation energy is 15.2 kcal/mol. This increase in growth rate above 500°C is unexpected and has not been observed previously.

The structural quality of InAs on GaAs grown at 410 or 425°C and V/III = 15 was examined by evaluation of the FWHM of DCXRD from the (400) reflection. The FWHM decreased with increasing InAs thickness from 450 arc sec for a 1- μ m-thick layer to 152 arc sec for a 5.5- μ m-thick layer grown at 410°C. Layers grown at 425°C had slightly larger x-ray linewidths. We speculate that the thickness

dependence is a result of a decreasing misfit dislocation density away from the epilayer-substrate interface, which is commonly observed for mismatched epitaxy. The mismatch between InAs and GaAs is 7%.

Hall measurement data showed that as the thickness of these undoped InAs layers increases the average electron mobility at 77 K increases as the square root of the thickness from 8×10^3 for a 0.3- μm -thick layer to $3.2 \times 10^4 \text{ cm}^2/\text{V s}$ for a 5.5- μm -thick layer, while the average electron concentration at 77 K decreases very rapidly from $\sim 2 \times 10^{17}$ to $1.6 \times 10^{16} \text{ cm}^{-3}$ over the same thickness range for a 410°C substrate temperature. This rapid decrease suggests a high donor concentration near the GaAs interface and a level below 10^{16} cm^{-3} away from the interface. Similar trends have also been observed in InAs epilayers on GaAs substrates grown by vacuum evaporation [14], atmospheric OMVPE [11], and molecular beam epitaxy [15]. The high value of mobility of $3.2 \times 10^4 \text{ cm}^2 \text{ V s}^{-1}$ and the corresponding electron concentration of $1.6 \times 10^{16} \text{ cm}^{-3}$ are better than any other values reported for OMVPE growth from TMIn and arsine, and are comparable to values for growth from TMIn and tertiarybutylarsine [12].

The effect of growth temperature on the electrical properties is shown in Figure 3-8(a) for 4- μm thick epilayers grown at temperatures in the range 400–425°C. The electron concentration measured at 77 K decreases with increasing temperature, while the mobility has a maximum at $\sim 410^\circ\text{C}$. In Figure 3-8(b), the effect of V/III ratio on the electron concentration and mobility is shown for epilayers grown at 410°C. The electron concentration increases from $1.2 \times 10^{16} \text{ cm}^{-3}$ for V/III = 7.5, to $2.8 \times 10^{16} \text{ cm}^{-3}$ for V/III = 20, while the mobility is a maximum of $3.0 \times 10^4 \text{ cm}^2 \text{ V s}^{-1}$ for V/III = 15.

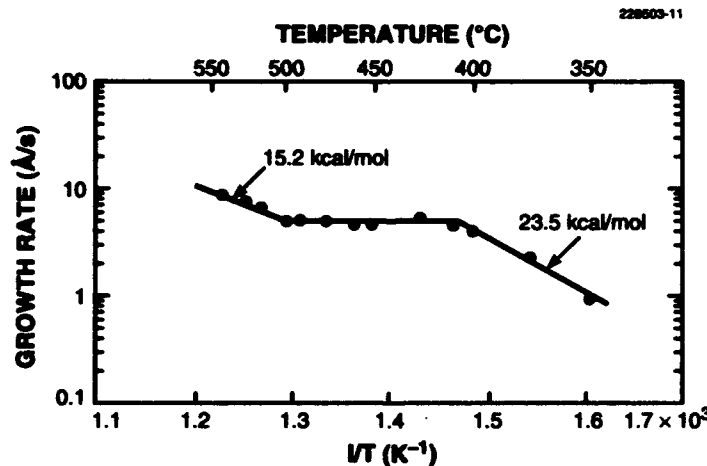


Figure 3-7. Dependence of InAs growth rate on substrate temperature.

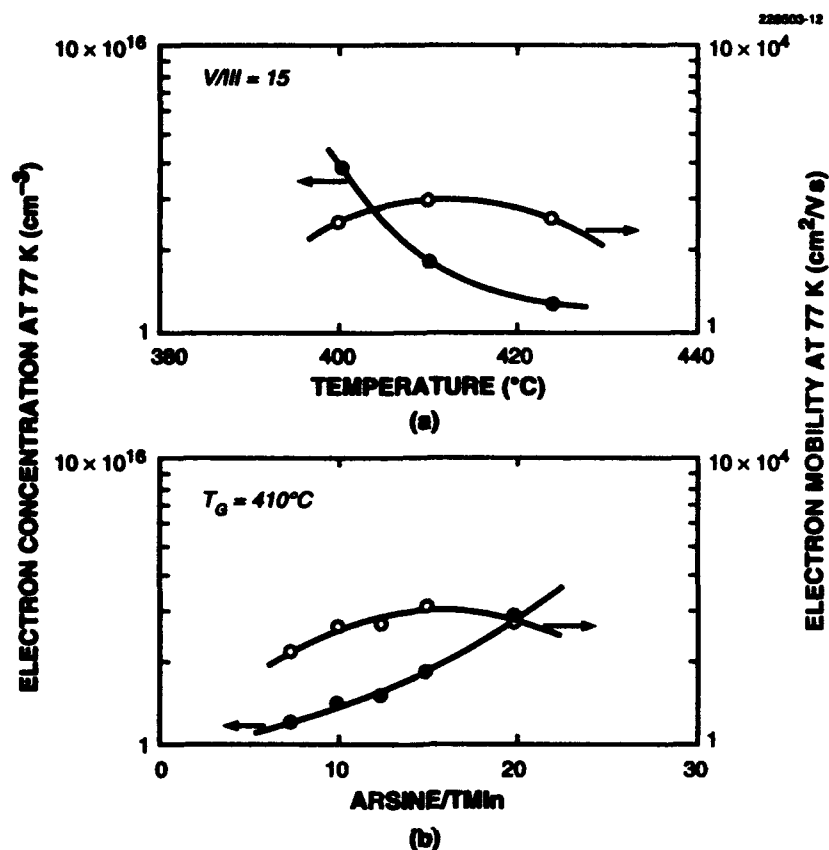


Figure 3-8. Electron concentration and mobility of InAs layers at 77 K as a function of (a) growth temperature and (b) V/III ratio.

The low-temperature PL spectra for layers grown in the temperature range 400–425°C and V/III ratio range 7.5–20 consisted of one dominant peak at 0.416 eV, which is attributed to the band-to-band emission. This value is similar to the energy reported by Ma et al. [13] for InAs grown on InAs substrates. The results of PL peak intensity normalized to the carrier concentration measured at 77 K are summarized in Figure 3-9 for 4- μm -thick epilayers. For epilayers grown at 410°C the normalized PL efficiency is a maximum for V/III = 15, as illustrated in Figure 3-9(a), and for epilayers grown with V/III = 15 the normalized PL efficiency increases with temperature, as seen in Figure 3-9(b).

C. A. Wang J. H. Reinold
J. W. Chludzinski D. R. Calawa

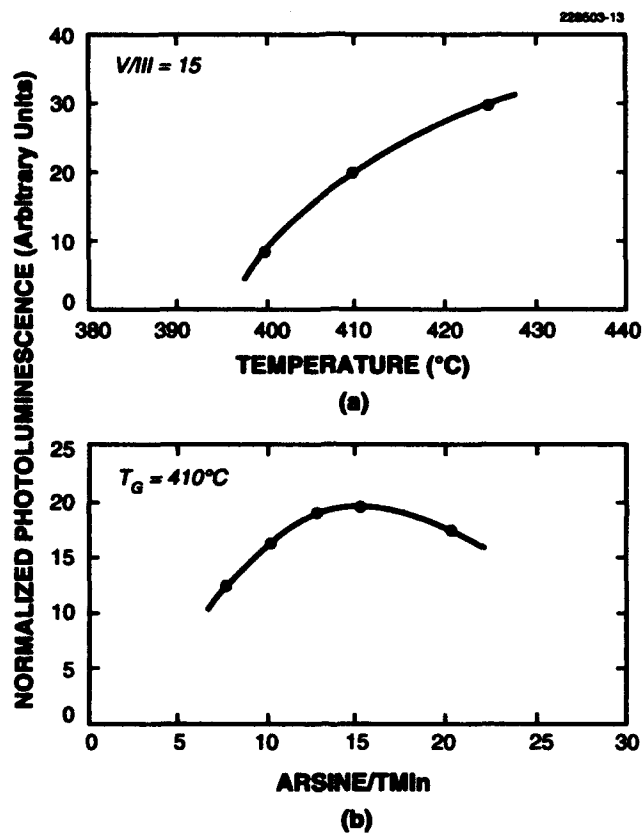


Figure 3-9. Normalized photoluminescence peak intensity of InAs layers as a function of (a) growth temperature and (b) V/III ratio.

REFERENCES

1. H. K. Choi and S. J. Eglash, *Appl. Phys. Lett.* **61**, 1154 (1992).
2. S. J. Eglash and H. K. Choi, *Proceedings of Lasers and Electro-Optics Society Annual Meeting* (IEEE, New York, 1992), p. 350.
3. A. E. Bochkarev, L. M. Dolginov, A. E. Drakin, P. G. Eliseev, and B. N. Sverdlov, *Sov. J. Quantum Electron.* **18**, 1362 (1988).
4. K. Peterman, *IEEE J. Quantum Electron.* **15**, 566 (1979).
5. M. Nakamura, K. Aiki, N. Chinone, R. Ito, and J. Umeda, *J. Appl. Phys.* **49**, 4644 (1978).
6. J. N. Walpole, E. S. Kintzer, S. R. Chinn, C. A. Wang, and L. J. Missaggia, *Appl. Phys. Lett.* **61**, 740 (1992).
7. J. N. Walpole, E. S. Kintzer, S. R. Chinn, C. A. Wang, and L. J. Missaggia, *Proc. SPIE* **1850**, 51 (1993).
8. D. Mehuys, L. Goldberg, R. Waarts, and D. F. Welch, *Electron. Lett.* **29**, 219 (1993).
9. R. Parke, D. F. Welch, A. Hardy, R. Lang, D. Mehuys, S. O'Brien, K. Dzurko, and D. Scifres, *IEEE Photon. Technol. Lett.* **5**, 297 (1993).
10. L. Goldberg, M. R. Surette, and D. Mehuys, *Appl. Phys. Lett.* **62**, 2304 (1993).
11. B. J. Baliga and S. K. Ghandi, *J. Electrochem. Soc.* **121**, 1642 (1974).
12. S. K. Haywood, R. W. Martin, N. J. Mason, and P. J. Walker, *J. Cryst. Growth* **97**, 489 (1989).
13. K. Y. Ma, Z. M. Fang, R. M. Cohen, and G. B. Stringfellow, *J. Electron. Mater.* **21**, 143 (1992).
14. N. Godinho and A. Brunnschweiler, *Solid-State Electron.* **13**, 47 (1970).
15. M. Yano, M. Nogami, Y. Matsushima, and M. Kimata, *Jpn. J. Appl. Phys.* **16**, 2131 (1977).

4. SUBMICROMETER TECHNOLOGY

4.1 SIMULATION OF SUB-0.25- μm RESIST PROCESSES FOR 193-nm LITHOGRAPHY

Resist processes including single-layer [1], bilayer [2],[3], and silylation resists [4] have been developed that incorporate chemistries suitable for 193-nm exposure. All three of these resist systems have sensitivity $< 50 \text{ mJ/cm}^2$ and demonstrate resolution to at least $0.20 \mu\text{m}$. This report describes the simulation techniques developed to predict process latitudes and dimensional bias during deep submicrometer integrated-circuit fabrication using these new processes.

The positive-tone single-layer resist process can be simulated using commercially available software, such as PROLITH/2 [5] or MCP [6]. Application of these models requires simply the experimental determination of key parameters for the new resist. To simulate surface-imaged resist systems, we have recently developed the MOSES (Modeling of Surface Exposed Systems) software. Like PROLITH/2 and MCP, MOSES is an empirical model and capable of simulating both bilayer [2],[3] and silylation [4] resist processes. The MOSES software together with commercially available models provide a simulation tool set for describing all the 193-nm resist approaches.

The MOSES model simulates the bilayer process by using an anisotropic development step for the imaging layer, followed by an anisotropic pattern-transfer step through the underlying planarizing films. An experimentally determined relationship between the rate of imaging layer development and the volumetric absorbed dose is used to simulate the resist development as a function of distance along the resist, depth into the resist, and time. The model can be used for wet- or dry-development processes. The algorithm for an oxygen plasma etch includes a rapid initial step where the surface portion (10–20 nm) of the organosilicon layer is consumed and converted into SiO_2 , followed by a slower steady-state erosion of the SiO_2 . The etch selectivities (imaging layer vs planarizing layer) and absolute planarizing layer etch rates have been experimentally determined using a parallel-plate reactive ion etcher, a magnetron etcher, an electron cyclotron resonance etcher, and a helical wave etcher [7]. The parameters used to describe any of these systems can be used as input into the pattern-transfer model.

In the silylation process, which is currently the most promising of the dry-developed resist processes, exposure to 193-nm radiation selectively crosslinks a layer 40–100 nm thick at the surface of the resist followed by selective diffusion of a silylating reagent of silicon into the unexposed areas of the resist. The incorporation of silicon increases the etch resistance to oxygen plasmas in these areas. The resulting silylation profile, which must be controllable in order to meet critical-dimension requirements, is dictated almost entirely by the silylating reagent diffusion characteristics rather than by the exposure profile [3]. One potentially deleterious result is isotropic diffusion of silylating reagent under the exposed (crosslinked) region. Figure 4-1 illustrates the effects of isotropic diffusion, which is most observable at silylation times several times longer than those used for standard processing.

These characteristics of the silylation process at 193 nm necessitate development of a silylation model not only to calculate process margins but also to develop a better overall understanding of the process limitations. Earlier attempts [8] to model this process, although successful, required a large number of experimentally obtained values. The earlier approach incorporates a parameter called the critical swelling stress, which is a function of exposure dose (degree of crosslinking) and silylation time

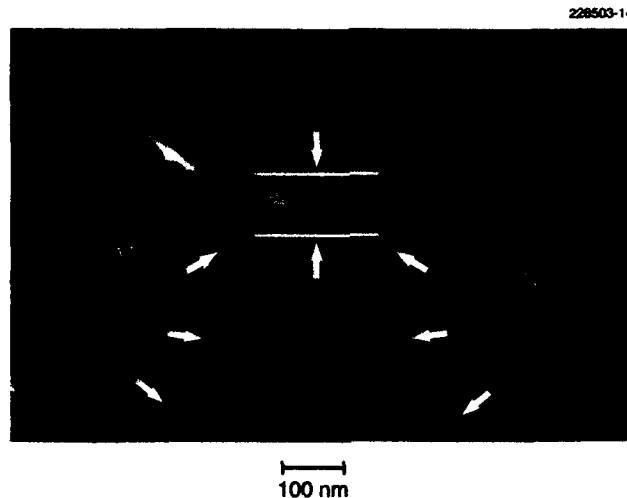


Figure 4-1. Cross-sectional scanning electron micrograph of oversilylated nominally 1.0-μm line-and-space structure imaged in poly(vinylphenol) at 193 nm. The silylation time was 5 min compared to a normal silylation time of 1–2 min. Note evidence of lateral diffusion by the silylating agent, which narrows the unsilylated width. The apparent silylation in the unsilylated area is a combination of gold (40 nm) deposited to prevent specimen charging in the electron microscope and a small amount of silylation (10–20 nm).

(degree of swelling). The parameter corresponds to the generated stress that would induce polymer crazing, after which the silylating agent transport rate would increase dramatically. This modeling approach, however, is limited by the uniqueness of the critical swelling stress for every combination of exposure dose and silylation time. To circumvent this, MOSES uses a depth-dependent silylating reagent diffusion rate, which qualitatively gives rise to a similar result, but relies on fewer empirical parameters and is easier to implement.

The MOSES model calculates these silylation profiles using an isotropic Case II diffusion model described by

$$dL/dt = KR(D)P \exp(-E/kT) , \quad (4.1)$$

where dL/dt is the silylation rate of any given volume element, K is a preexponential constant, P is the silylating agent pressure, E is the activation energy for diffusion (as dictated by polymer relaxation for Case II diffusion), k is Boltzmann's constant, T is the temperature, $R(D)$ is the experimentally determined dose-dependent diffusion rate normalized relative to the diffusion rate in unexposed polymer [(where $R(0) = 1$)], and D is the volumetric absorbed dose in units of mJ/cm^3 . Of these variables, all are experimentally measurable except for K , which is determined from the slope of a plot of experimentally measured L vs t data.

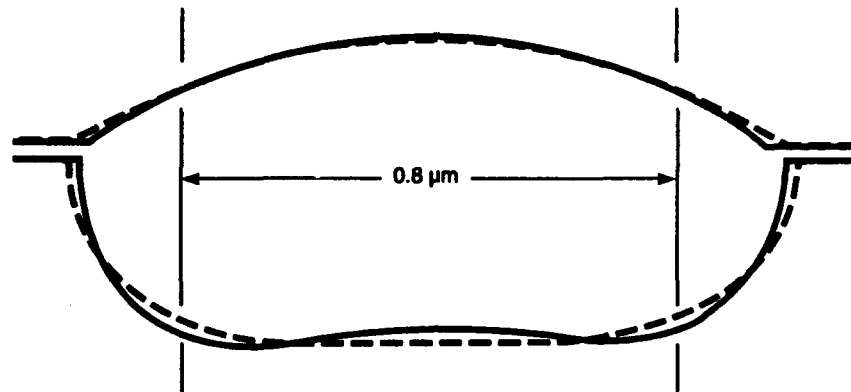


Figure 4-2. Comparison of MOSES silylation model (dashed line) with an experimentally measured silylation profile (solid line). The resist was poly(vinylphenol), the simulated exposure dose was 80 mJ/cm^2 , and the silylation conditions were 105°C , 1.5 min, 10 Torr. The model assumed diffraction-limited optics, whereas the experimental image quality was limited by aberrations. The differences in aerial image may account for the differences in profile. For the experimental exposure, the fluence per pulse was calibrated at $\sim 0.25 \text{ mJ/cm}^2$ per pulse.

The shape of the swollen surface that results from the volume expansion upon silylation is assumed to be controlled by surface tension, because at these silylation temperatures the surface tension is sufficient to induce mechanical deformation in the swollen resist [9]. Given a fractional expansion coefficient (typically 40–50%) that occurs after the incorporation of the silylating reagent, we determine the increase in area that would be necessary to describe this swelling and then create a circular surface profile having the appropriate area. A circular profile is chosen because it, like the cross section of a profile controlled by surface tension, has a minimum surface length. This approach has worked well for simple structures and has been confirmed experimentally.

Figure 4-2 shows MOSES output compared to an experimentally obtained silylation profile. The comparison is made for an oversilylated feature to allow better measurement of the experimental profile. The differences between the experimental and simulated profiles are attributed either to discrepancies between the theoretical and actual aerial images or to diffusion anomalies related to stress. In either case, the agreement is quite good, indicating that the MOSES silylation model provides a close approximation to actual resist performance under our experimental conditions. Currently, MOSES is being used in development of the silylation process as an aid in determining the optimal experimental conditions. These results shorten the process development cycle by identifying those conditions which lead to maximum process margins. In time, the silylation process will allow fabrication of sub-200-nm design-rule devices over a $22 \times 35\text{-mm}$ field using an advanced 193-nm exposure tool.

R. R. Kunz
M. A. Hartney
R. W. Otten, Jr.

4.2 EVALUATION OF DEPTH OF FOCUS IN PHOTOLITHOGRAPHY AT 0.25 μm

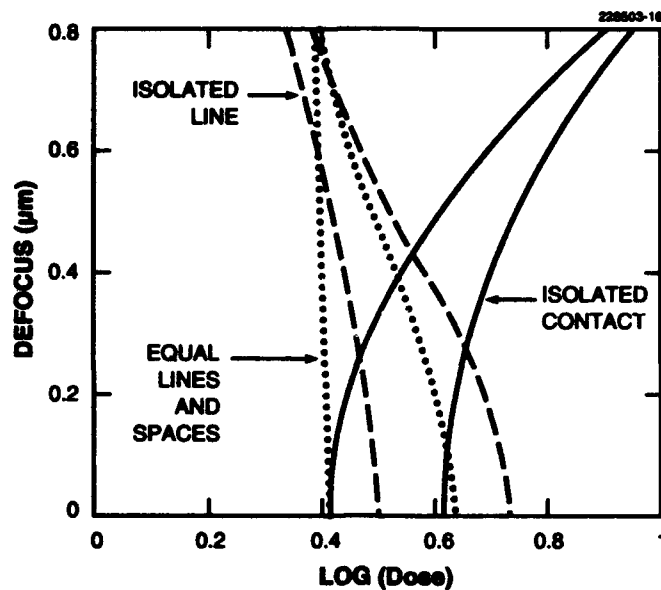
The design of optical lithography systems requires the optimization of resolution, depth of focus (DOF), and exposure latitude. To express the minimum linewidth (LW) and DOF in terms of the actinic wavelength λ and the numerical aperture (NA) of the imaging optics, two rules of thumb are commonly used: (1) $\text{LW} = k_1 \lambda / \text{NA}$ and (2) $\text{DOF} = \pm k_2 \lambda / (\text{NA})^2$. In these expressions k_1 and k_2 are process parameters, independent of λ and NA. From basic principles k_1 must be > 0.25 (in practice it is ~ 0.5 to 0.8), but there are no fundamental limitations on the value of k_2 . The Rayleigh DOF, $k_2 = 0.5$, is frequently used for quick estimates. The accuracy of this approach is limited because it takes into account neither the degree of spatial coherence of the illumination optics nor the effects of feature type and proximity in the complex patterns of realistic circuits. It also fails to provide information on the exposure latitude.

The availability of fast computers and efficient algorithms makes it practical to simulate the aerial image of complex patterns from first principles and to evaluate the DOF and exposure latitude under a range of imaging alternatives. Here, we present results of modeling the performance of exposure tools designed for 0.25- μm geometries. These dimensions correspond to 256-Mbit dynamic random access memory chips which are expected to go into production in 1998. In particular, the relative advantages of 248- and 193-nm systems, with and without off-axis illumination, are explored.

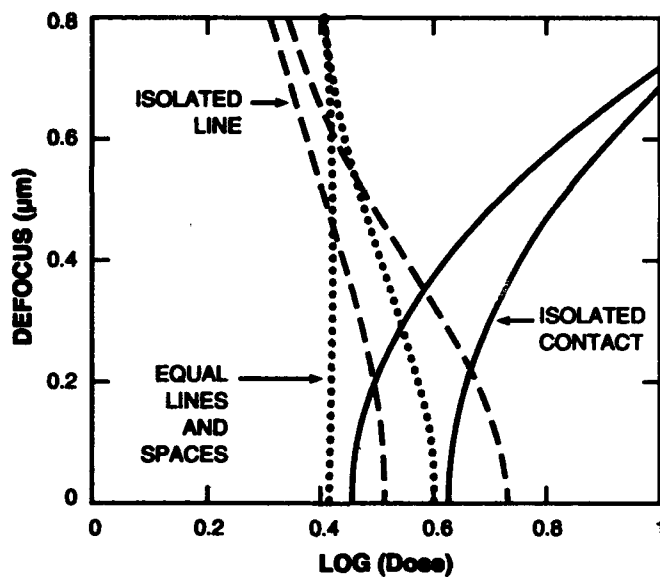
The software [10] employed calculates the aerial image by solving Maxwell's equations and can use either the scalar or vector representation of the electric field. The effect of aberrations can be calculated by introducing Zernike polynomials, although in our study we assumed diffraction-limited performance throughout. The most remarkable feature of this software, however, is its speed. The aerial image of complex masks as large as a full functional cell can be calculated on a state-of-the-art workstation within less than 15 min. Furthermore, the time required to calculate the aerial image increases only linearly with the area, rather than showing the quadratic dependence used in other algorithms. Thus, the performance of exposure tools with realistic mask levels can be evaluated within short periods of time.

We simulated the aerial image of 3- μm -long equal lines and spaces, a 3- μm -long isolated line, and an isolated contact hole. Then, the intensity distribution across the center of each feature was calculated. All features were 0.25 μm wide. It should be noted that at these dimensions, which are close to the wavelength, an isolated contact hole behaves quite differently from an isolated space. By using the one-dimensional intensity profile across the center of each type of structure, we constructed exposure-defocus (E-D) plots [11]. Figure 4-3 shows examples of E-D plots obtained with a $\pm 10\%$ allowed variation on the 0.25- μm feature size, with Figure 4-3(a) representing a 193-nm, 0.5-NA system and 4-3(b) a 248-nm, 0.65-NA system. The value of 0.65 in the latter was chosen so as to keep the k_1 factor the same as for the 193-nm tool, and therefore the exposure latitudes at zero defocus are nearly the same for both systems. However, the 248-nm, high-NA system clearly has a lower DOF, as illustrated by the more rapid bending and narrowing of the E-D plots. This result is in qualitative agreement with the Rayleigh expression, but it reveals further information about the exposure latitude and how it impacts on DOF.

Since maximizing the DOF is our main concern, we further reduced the E-D data by imposing an exposure latitude requirement of $\pm 10\%$, without specifying the mean value. The value of the mean dose was selected with reference to the specific E-D plot (and therefore could be different for the different feature types), in such a way as to maximize the allowable defocus value. In the following we refer to twice the defocus value thus obtained as the DOF. (The factor of 2 is introduced to account for allowable



(a)



(b)

Figure 4-3. Exposure-defocus (E-D) plots of aerial image of equal lines and spaces, an isolated line, and an isolated contact hole, representing exposure (a) at 193 nm with 0.5 numerical aperture (NA) and coherence factor $\sigma = 0.6$, and (b) at 248 nm with 0.65 NA and $\sigma = 0.6$. The nominal feature size was $0.25 \mu\text{m}$, and a $\pm 10\%$ linewidth control was used throughout. The dose values were normalized to that required for open field exposure. The usable E-D parameter space for each feature type is enclosed between its two corresponding lines and the x-axis.

defocusing in both directions.) It should be noted that this definition of DOF, namely, within the constraints of $\pm 10\%$ LW control and $\pm 10\%$ exposure dose, is quite different from the conventional DOF, which does not allow for exposure variation.

With the above definition of DOF, the parameters of the 248-nm exposure system were allowed to vary over a wider range. While the wavelength and the reduction ratio were kept fixed, the NA was varied in the range 0.40–0.75, the coherence factor s was varied from 0.3 to 0.7, and annular illumination was introduced with a range of inner and outer radii. Some of the results are shown in Figures 4-4 and 4-5. It is seen that the optimal values of NA and s depend on the feature type. For instance, under conventional (circular) illumination and with $s = 0.6$, the optimal NA for equal lines and spaces is 0.45 at 193 nm and 0.50 at 248 nm. However, for isolated contacts the dependence of DOF on NA is much less pronounced, with the optimal NA ~ 0.50 at 193 nm and ~ 0.65 at 248 nm.

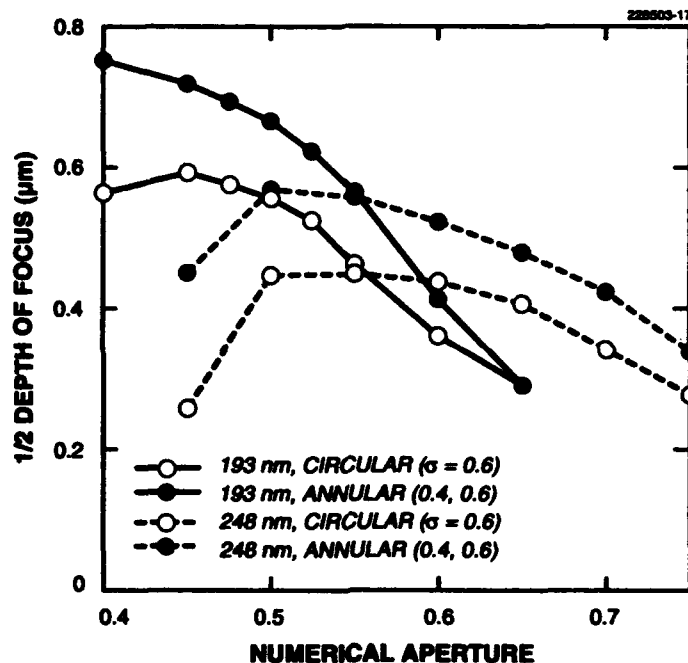


Figure 4-4. Calculated depth of focus (DOF) of the aerial image of 0.25- μm equal lines and spaces, as a function of NA of the exposure tool. Two wavelengths are used in the simulation, 193 and 248 nm, each under two illumination conditions: circular with $\sigma = 0.6$, and annular with inner and outer radii, respectively, of 0.4 and 0.6, normalized to the maximum viewable source size.

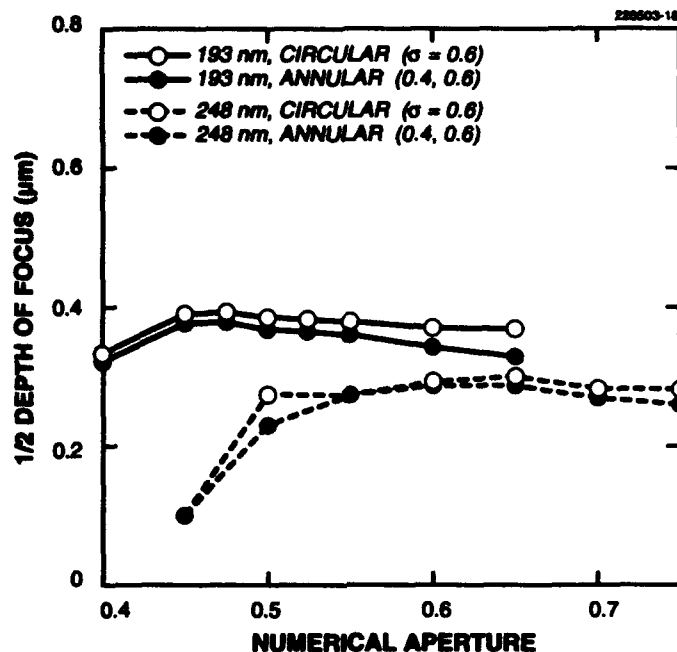


Figure 4-5. Calculated DOF of the aerial image of 0.25- μm isolated contact hole. The exposure conditions are as in Figure 4-4.

Equally significant is the variation of the DOF with feature type. A 193-nm, 0.5-NA system yields DOF of 1.1 and 0.80 μm for equal lines and spaces and for an isolated contact, respectively. A 248-nm, 0.65-NA system has 0.8- and 0.6- μm DOF for the same features, respectively. Furthermore, with conventional (circular) illumination the DOF of the unoptimized 193-nm system is always better than that of a 248-nm tool (except for equal lines and spaces at $\text{NA} > 0.55$). The introduction of annular illumination to the 248-nm, 0.5-NA tool does increase its DOF to that of a conventionally illuminated 193-nm system, but only for the dense pattern of equal lines and spaces. In fact, annular illumination has a significant negative impact on the DOF when isolated lines are to be printed. This result is qualitatively understood in terms of the Fourier components of the respective patterns. In the case of equal lines and spaces the dominant components have high frequencies and are enhanced by the annular illumination. However, in isolated features low-frequency components contribute to the final image as well, and these are repressed by the annular illumination.

M. Rothschild
S. P. Doran
E. Barouch*

U. Hollerbach*
S. A. Orszag*

*Author not at Lincoln Laboratory.

REFERENCES

1. R. R. Kunz, R. D. Allen, W. D. Hinsberg, and G. M. Wallraff, to be published in *Proc. SPIE* **1925** (1993).
2. R. R. Kunz, M. W. Horn, R. B. Goodman, P. A. Bianconi, D. A. Smith, and J. R. Eshelman, *J. Vac. Sci. Technol. B* **10**, 2554 (1992).
3. R. R. Kunz, M. W. Horn, R. B. Goodman, P. A. Bianconi, D. A. Smith, J. R. Eshelman, G. M. Wallraff, R. D. Miller, and E. J. Ginsberg, *Proc. SPIE* **1672**, 385 (1992).
4. M. A. Hartney, D. W. Johnson, and A. C. Spencer, *Proc. SPIE* **1466**, 238 (1991).
5. C. A. Mack, *Proc. SPIE* **538**, 207 (1985).
6. E. Barouch, B. Bradie, U. Hollerbach, S. A. Orszag, and M. Peckerar, *Proc. SPIE* **1465**, 586 (1991).
7. M. W. Horn, M. A. Hartney, and R. R. Kunz, *Proc. SPIE* **1672**, 448 (1992).
8. M. A. Hartney, *J. Vac. Sci. Technol. B* **3**, 681 (1993).
9. R. R. Kunz, M. A. Hartney, R. W. Otten, Jr., E. Barouch, U. Hollerbach, and S. Orszag, to be published in *Proc. SPIE*.
10. D. C. Cole, E. Barouch, U. Hollerbach, and S. A. Orszag, *J. Vac. Sci. Technol. B* **10**, 3037 (1992); B. Kuyel, E. Barouch, U. Hollerbach, and S. A. Orszag, *Proc. SPIE* **1674**, 376 (1992).
11. B. J. Lin, in *Microcircuit Engineering 89: Proceedings of the International Conference on Microlithography* (Elsevier, New York, 1990), p. 137.

5. HIGH SPEED ELECTRONICS

5.1 QUALITATIVE MODEL FOR THE CURRENT STABILITY OF HYDROGEN-PASSIVATED MOLYBDENUM FIELD-EMISSION CONES

Analysis of the field-emission data from molybdenum cones indicates that unpassivated cones lack the current stability required to produce useful vacuum microelectronic devices. This has led to the development of a number of schemes for passivating the cones. Although none of these methods are well understood, hydrogen passivation has been the most successful to date and therefore the most widely used [1],[2]. In an endeavor to explain this phenomenon better, we have recently used a high-resolution transmission electron microscope (TEM) to study the detailed structure of the tips of our molybdenum field-emission cones [3]. From the results of this study along with related data from the literature, we propose a qualitative model for the current stability of such cones both with and without hydrogen passivation.

The TEM micrographs of end sections of typical cones revealed two important structural properties. First, the tips have a somewhat irregular shape: some have one sharp primary protrusion and sharp secondary protrusions with radii ~ 1 nm, while others are more blunt with the radii of protrusions being > 3 nm. Second, the average size of the grains forming the tips is ~ 5 – 10 nm. It is probably these grains that cause the irregular shapes.

In our earlier report we discussed the significance of the small protrusions [3]. Here we focus on the grain structure at the tips of the cones to develop our model. To understand some of the implications of having a small molybdenum grain structure, it was necessary to review literature from the steel industry relating to molybdenum. The crystalline structure of molybdenum is body centered cubic, and in polycrystalline molybdenum precipitates of hydrogen, oxygen, nitrogen, and carbon coalesce preferentially along grain boundaries [4]. Furthermore, impurities such as hydrogen are able to preferentially diffuse into polycrystalline molybdenum along grain boundaries [5]. The effect of adding hydrogen, oxygen, nitrogen, and carbon to the grain boundaries is to cause embrittlement, i.e., to raise the plastic deformation temperature and severely reduce grain slip. Since the hydrogen passivation of field emitters is of interest, it is relevant to consider the effects produced by forcing hydrogen through polycrystalline molybdenum and molybdenum alloys. Armacanqui and Oriani [6] indicate that when hydrogen is forced through grains using electrolytic charging, an increased number of defects also coalesce at the grain boundaries. Under proper conditions the defects can cause the grains to deform, and in severe cases in the absence of external forces to fail, creating microcracks. Furthermore, Prekel and Lawley [7] and Noda et al. [8] suggest that, with proper control, hydrogen can be used to reduce other contaminants such as oxygen and carbon. Work by Schwoebel et al. [2] on the hydrogen passivation of field-emission cones indicates that plasma hydrogen can be used to reduce current instability and increase current density.

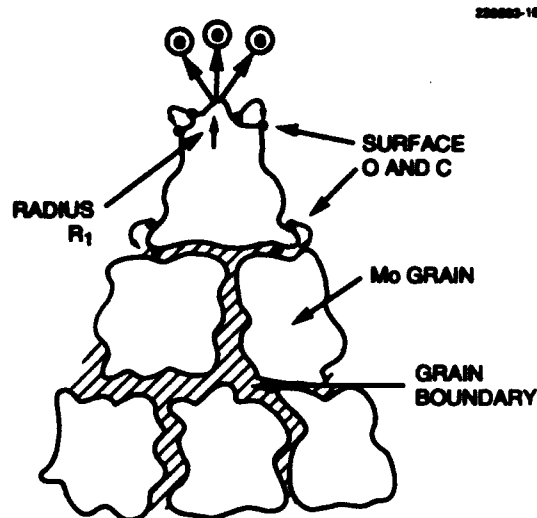
Our model is formulated for the two cases of emitter operation without hydrogen passivation and after hydrogen passivation. The non-hydrogen-passivated case is discussed first. Figures 5-1(a) and 5-1(b) show schematic diagrams of an unpassivated tip at low and high current levels, respectively. At low current levels the structure is stable with no movement of the grains. The initiation of current from a small

protrusion on the tip of the cone causes some movement of surface carbon and oxygen to the grain boundaries. As more current is extracted, the protrusion heats resulting in increased surface migration to the grain boundaries. The increased current also causes ohmic heating of the grain boundaries, especially those near the surface of the cone. The defects in the grains and the contaminants in the boundaries cause the grains to shift and deform, establishing a new minimal free energy for the system. A shift in emission current follows as the field emission switches to another protrusion with a different radius of curvature. The result is an uncontrolled change in emission current. As the current is increased the process repeats until ionized desorbed contaminants establish an arc and the structure fails. With this model, devices are more stable under ultrahigh-vacuum conditions than high-vacuum conditions, since the shifting process stops once surface oxygen and nitrogen are tied into the structure. Under high-vacuum conditions a reservoir of hydrogen, oxygen, nitrogen, and carbon is available to continue and rebalance the process.

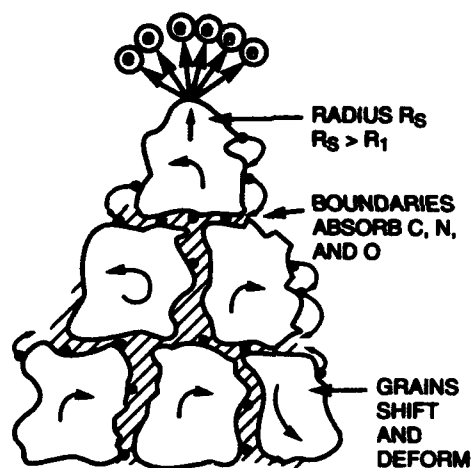
Figure 5-2 shows several schematic diagrams relating to the hydrogen passivation of tips. The hydrogenation process, illustrated in Figure 5-2(a), consists of bombarding the surface of the cone with hydrogen ions generated in a hydrogen plasma [2]. The bombardment causes the desorption of surface oxygen, carbon, and hydrogen passivates all grain boundaries in the tip area. The process in effect "locks" the structure into a specific minimal free energy state. As shown in Figure 5-2(b), the locked structure is very stable at a variety of current levels and with local thermal load as compared to the unpassivated structure. Furthermore, vacuum conditions are not as important since all grain bonds have been tied up. With the structure fixed, high extraction currents can now be applied to field-form an atomic emitter, as illustrated in Figure 5-2(c).

The intent of this model is to focus on the interrelationship between the grains, grain boundaries, contaminants, and current stability. In early noise studies, Spindt et al. [9] suggested that single-atom effects contribute to the noise characteristics of polycrystalline molybdenum devices. They also suggested that effects due to vibrational levels generated at emitter operation temperatures are important. In fact, all these effects contribute to current fluctuations and require further study.

W. D. Goodhue	D. D. Rathman
P. M. Nitishin	G. D. Johnson
C. T. Harris	M. A. Hollis
C. O. Bozler	



(a)



(b)

Figure 5-1. Schematic diagrams of nonhydrogenated tips. (a) Tip during low-current operation. At low current levels the structure is stable even though some surface contaminants diffuse into the grains. (b) Tip during high-current operation. At high current levels, surface impurities and vacuum quality affect the amount of contaminants diffusing into the grains, causing shifts in grain configuration and changes in device operation.

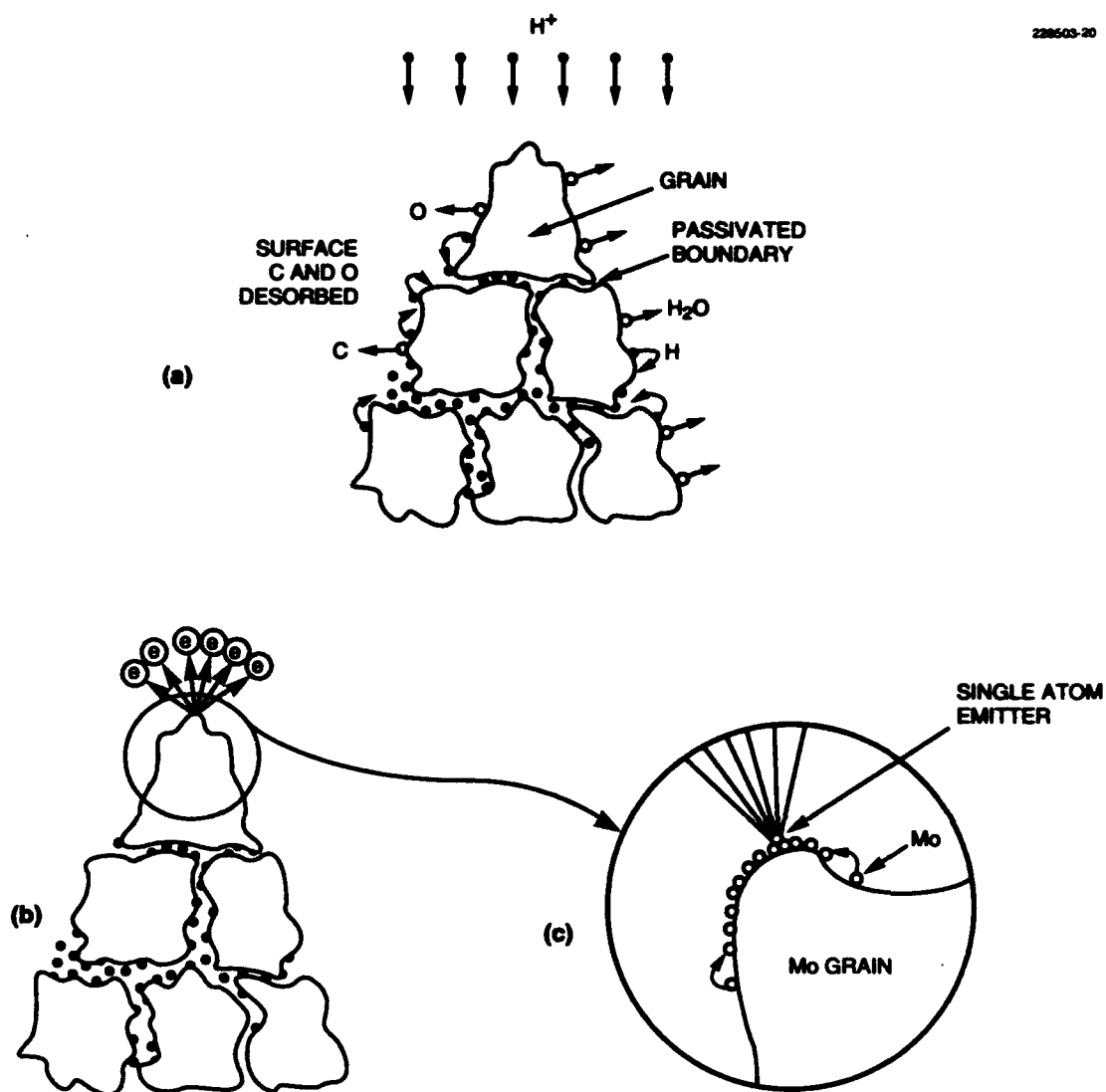


Figure 5-2. Schematic diagrams of the hydrogenation process and resulting tip structure. (a) The plasma hydrogen process removes surface oxides and carbons and supplies hydrogen which diffuses into the grain boundaries to stabilize the structure. (b) After hydrogenation the structure is stable at a variety of current levels since all dangling bonds in the grain boundaries near the tip have been passivated. (c) The structure remains stable even at current levels as high as those required to field-form an atomic emitter.

REFERENCES

1. M. S. Mousa, C. E. Holland, I. Brodie, and C. A. Spindt, *Appl. Surf. Sci.* **67**, 218 (1993).
2. P. R. Schwoebel, I. Brodie, and C. A. Spindt, in *Sixth International Vacuum Microelectronic Conference Technical Digest* (IEEE, New York, 1993), p. 14.
3. Solid State Research Report, Lincoln Laboratory, MIT, 1992:4, p. 29.
4. D. P. Shashkov, *Fiz. Met. Metalloved.* **26**, 110 (1968).
5. M. Taheri, *Mater. Sci. Eng.* **32**, 221 (1978).
6. M. E. Armacanqui and R. A. Oriani, *Mater. Sci. Eng.* **91**, 143 (1987).
7. H. C. Prekel and A. Lawley, The Franklin Institute Research Laboratories Report IB21951, 1965.
8. T. Noda, T. Kainuma, and M. Okada, *Trans. Natl. Res. Inst. Metals* **28**, 231 (1986).
9. C. A. Spindt, I. Brodie, L. Humphrey, and E. R. Westerberg, *J. Appl. Phys.* **47**, 5248 (1976).

6. MICROELECTRONICS

6.1 MODELING OF CHARGE PACKET DIFFUSION IN THE FIELD-FREE REGION OF A THINNED BACK-ILLUMINATED CHARGE-COUPLED DEVICE

A photoelectron, or in the case of x-ray excitation a packet of photoelectrons, generated in a charge-coupled device (CCD) may diffuse laterally before being collected in the buried channel of a pixel. If the photoelectron crosses a boundary from one pixel into another, then an error will occur in counting the number of photons absorbed in each of those pixels. This lateral diffusion depends primarily on pixel size, the thickness of the Si that absorbs photons, and the electric field. Calculations have been made of the extent of the diffusion under conditions that simulate absorption of photons in the undepleted region of a thinned, back-illuminated CCD, where the electric field is zero. This corresponds to a worst-case estimate for charge spreading, since the electric field in the depleted region will drive a photoelectron created here toward the buried channel and suppress lateral diffusion.

The thickness of the field-free region is assumed to be uniform, that is, the effect of channel stops and differing potentials applied to the CCD gates is ignored. A $24 \times 24\text{-}\mu\text{m}$ pixel is assumed to be centered in the x - y plane at the origin, with the edge of the depleted region at $z = 0$. The field-free region extends in the positive z direction for a thickness d_s , with the photon absorbed at a height z_s . The calculations are based on the method of images applied by Hopkinson [1], assuming reflection with no recombination at $z = d_s$, no recombination in the bulk, and a perfect sink at $z = 0$. Figure 6-1(a), which displays an array of 3×3 pixels centered at (0,0), shows the result of one calculation for a photon absorbed at the top of a $9\text{-}\mu\text{m}$ -thick region, that is, $z_s = d_s = 9\text{ }\mu\text{m}$. This corresponds to a thinned CCD fabricated on Si of $40\text{-}\Omega\text{ cm}$ resistivity (depletion width $8\text{ }\mu\text{m}$) with a total thickness of $17\text{ }\mu\text{m}$, being back illuminated by blue or ultraviolet (UV) light. The contours correspond to the probability that an electron generated at a location in the x - y plane will be collected in the pixel centered at (0,0). The behavior of the electron collection is nearly Gaussian, as seen in Figure 6-1(b), but a fourfold symmetry imposed by the array of square pixels is exhibited, which is most apparent near the origin. The peak response at the origin is ~ 0.73 , and as indicated in Figure 6-1(a), the full width at half-maximum (FWHM) is close to the size of the pixel, suggesting that most of the charge is collected by the pixel where the electron was generated.

The results of other calculations are shown in Table 6-1, which contains information on the maximum response and the percentage of charge absorbed by the central pixel. In all cases the amount of charge collected by each of the four nearest neighbor pixels is < 0.10 , while that collected by each of the four next nearest neighbors is < 0.05 .

These values of d_s and z_s correspond to cases of interest for thinned devices of different thickness, resistivity, and wavelength of the illuminating light. The value for d_s will increase either as the total thickness of the thinned CCD increases or as the resistivity goes down; for typical thinned devices fabricated on $40\text{-}\Omega\text{ cm}$ material with a total thickness of $17\text{ }\mu\text{m}$, a value of d_s of $9\text{ }\mu\text{m}$ is most appropriate. Photons in the blue or UV may be assumed to be absorbed at the back surface of the illuminated CCD, that is, where $d_s = z_s$.

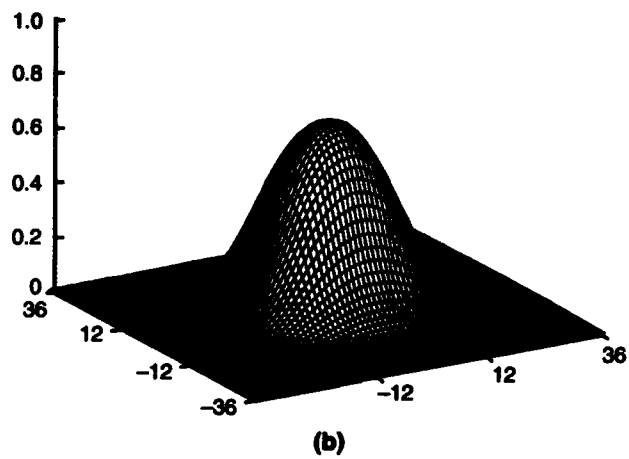
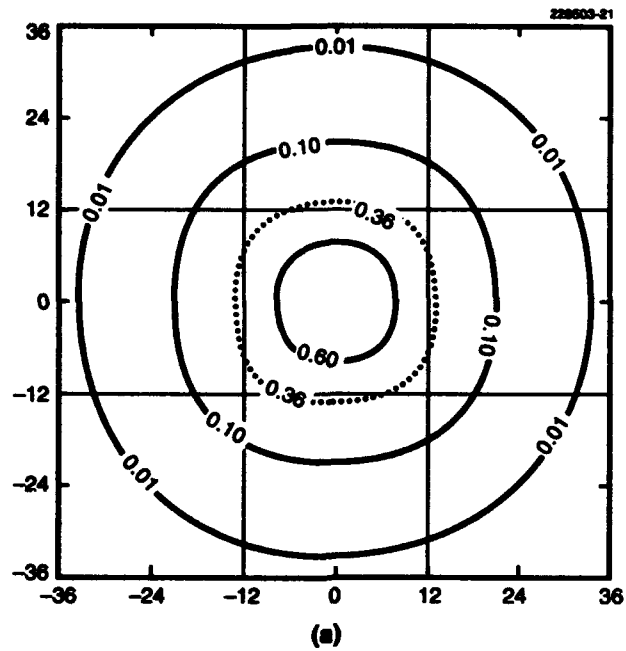


Figure 6-1. Probability of charge collection by central $24 \times 24\text{-}\mu\text{m}$ pixel illustrated by (a) contour plots and (b) a three-dimensional view. The dashed curve in (a) is the full width at half-maximum.

TABLE 6-1

Collection of Charge Diffusing in Field-Free Region of CCDs

d_s (μm)	z_s (μm)	Maximum	Charge Collection in Central Pixel
4	4	0.98	0.77
9	3	0.86	0.69
9	4.5	0.81	0.62
9	9	0.73	0.54
14	4.7	0.72	0.55
14	7	0.62	0.47
14	14	0.49	0.37
18	9	0.50	0.38
18	18	0.35	0.29

It is apparent from Table 6-1 that as the thickness of the field-free region in the device increases from 4 to 18 μm , the maximum probability of charge collection at the center for electrons generated at the back surface decreases by about a factor of 3 as does the fraction of the charge collected in the central pixel. The FWHM of these cases increases from 24 to 34 μm . This difference in FWHM due to differing thicknesses of Si may be compensated to some degree by using charge centroiding among nearest neighbor and next nearest neighbor pixels, so that the point of origin of the photoelectron may still be determined accurately.

Table 6-1 also indicates that for a given d_s , the response improves for lower values of z_s , that is, as the photoelectron is generated closer to the edge of the depletion region at $z = 0$. This response depends only weakly on z_s , so for the case of $d_s = 9 \mu\text{m}$, an electron generated by a UV photon absorbed at the surface ($z_s = 9 \mu\text{m}$) of the central pixel has a 54% probability of being collected in this pixel, while an electron generated at $z_s = 3$ (by a near-infrared photon with a wavelength of 850 nm or an x-ray with a wavelength of 1 nm) has a 68% probability of being collected by the central pixel.

Overall, the thickness of the field-free region in a thinned device does not appear to seriously limit the accuracy of locating UV and infrared photon absorption within the CCD. Preliminary results of measurements indicate good agreement with these calculations [2].

J. A. Gregory
N. E. Altaffer
R. D. Kent

REFERENCES

1. G. R. Hopkinson, *Opt. Eng.* **26**, 766 (1987).
2. B. E. Burke, H. R. Clark, Jr., and R. K. Reich, private communication.

7. ANALOG DEVICE TECHNOLOGY

7.1 TEST CIRCUIT FOR DUAL-ANALOG-TERNARY CORRELATOR

A self-contained compact low-power test circuit has been developed for the mixed-signal dual-analog-ternary correlator (2ATC) chip. The 2ATC is an application-specific integrated circuit designed at Lincoln Laboratory and fabricated commercially using a 2- μ m CMOS/charge-coupled-device process. The chip was developed for NASA's upgrade of their advanced tracking and data-relay satellite system, where it will support multiple spread-spectrum communication modes of operation. To demonstrate the more general applicability of the 2ATC, a circuit was developed to provide a quick and easy, yet comprehensive, test vehicle for the device. Since this circuit provides code-like signals to the 2ATC and can be configured in a compact pocket-sized format, it has been named Codeman. With a zero-insertion-force socket, it provides an ideal mechanism for quick device screening.

The signals generated by Codeman and input to the 2ATC produce outputs with characteristics that allow for the ready determination of device quality, while also providing a means to monitor the deterioration of a device under stressful conditions. Although the maximum charge-coupled device clocking rate of the 2ATC exceeds 50 MHz, Codeman is not intended to characterize performance at these high rates. High speed was traded for minimum size and power with maximum simplicity and functionality. The result is a design that operates at a maximum rate of about 10 MHz using standard off-the-shelf groupings of logic elements available from a number of different logic families.

The design encompasses a total of ten chips, which generate all of the signals required to verify proper performance of the two 256-tap 2ATC main correlators. (Two additional 12-tap companion correlators accompanying the main correlators are kept disabled.) The logic family chosen for the prototype boards was advanced low-power Schottky TTL, since this provided a high level of performance with low power dissipation. Figure 7-1 shows one of these prototype Codeman circuits with an embedded 2ATC device. The printed-circuit board is a multilayer design, and the entire circuit draws < 1.5 W from a 5-V supply. About 1 W of this power is consumed by the 2ATC itself, which also requires a minimal amount of power from a -5-V supply for substrate bias.

Figure 7-2 shows a 2ATC input generated by the Codeman prototype of Figure 7-1 for one complete programming cycle. Figure 7-3 shows the corresponding correlator output. Correlator tap weights are programmable to +1, -1, or zero. During one half cycle the correlator tap weights are programmed by Codeman to match the incoming signal. The input consists of a continuous stream of 255-bit bipolar (plus and minus) codes spaced by equivalent-duration (zero) dead times. The code repeatedly cycles over four patterns: pseudo-noise, pseudo-noise complement (plus to minus and minus to plus), square wave, and square-wave complement. Inputs of pseudo-noise codes produce spike-like autocorrelations at the output, while outputs for square-wave inputs are triangular. A malfunction of a single tap within a correlator manifests itself as a corresponding jog in an otherwise smooth triangular output autocorrelation. During the other half cycle, Codeman programs only a single correlator tap weight so that the output becomes a delayed version of its input. Tap weights are programmed to a particular pattern for one input code and the complementary pattern for the following complementary input. Therefore, since the single

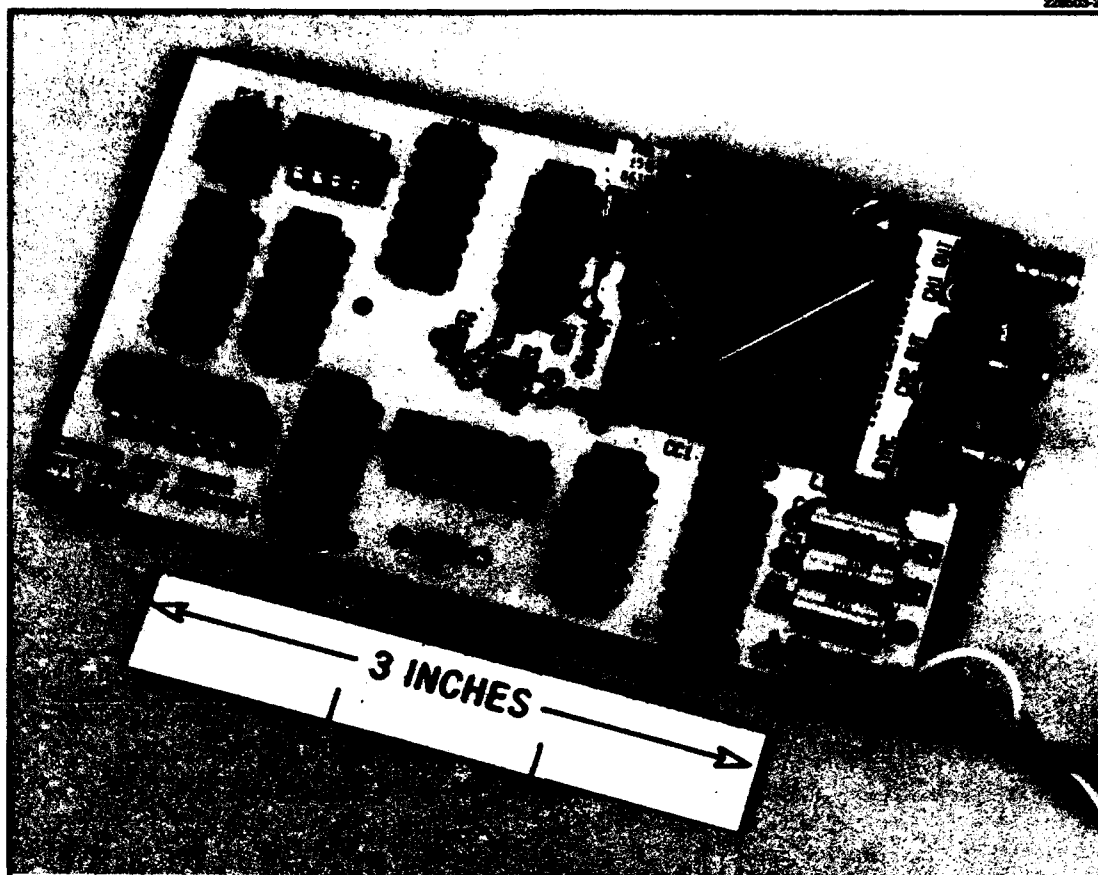
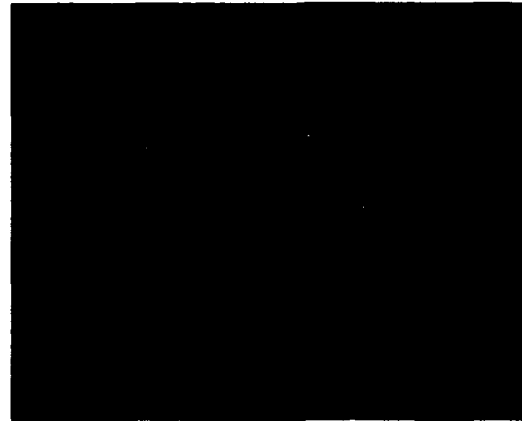


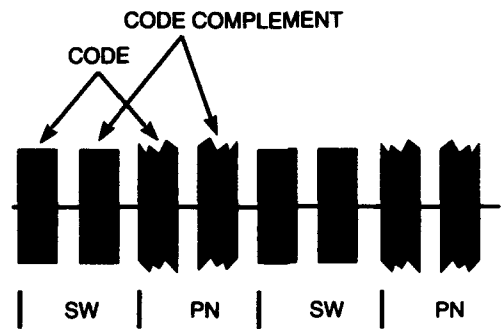
Figure 7-1. Multilayer version of Codeman with 2ATC in a standard socket. The circuit uses ten low-power off-the-shelf components for the generation of signals to the 2ATC device.

tap in the delay-line half cycle is the unused tap of the autocorrelation half cycle, during one complete cycle all taps are programmed into all possible states.

D. R. Arsenault
M. M. Seaver
T. J. Weir



(a)

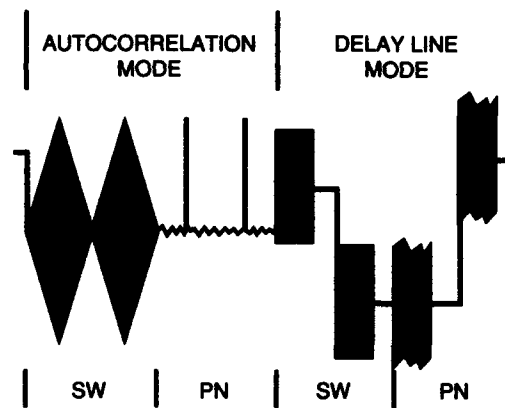


(b)

Figure 7-2. (a) Photographic and (b) graphic versions of output from Codeman circuit over a complete cycle. This output is input to a 2ATC device under test. The square-wave (SW) and pseudo-noise (PN) code progression is indicated in (b).



(a)



(b)

Figure 7-3. (a) Photographic and (b) graphic versions of 2ATC output over a complete cycle resulting from stimulation by Codeman-generated signals. The SW and PN correlation types are indicated in (b).

7.2 HIGH-POWER-HANDLING YBCO FILMS

The low microwave losses and consequent high- Q resonant structures provided by thin-film superconductors used in bandpass filters and channelizers promise advantages in communication, radar, and signal-intercept systems. Through the use of the superconductors many microwave components can be implemented having almost ideal characteristics. Steady progress has been made by several research and development teams in producing acceptably low-loss large-area films, and a variety of devices have been demonstrated, such as oscillators, demodulators, and channelizers.

Most of the work to date has concentrated on low-power applications. While the low losses at low power are a necessary condition for the material to be useful in real applications, practical systems frequently require higher power levels. In particular, the majority of filter applications will require the ability to handle power levels higher than reported to date. Typical results show a power-handling capability of ~ 100 mW. Obviously, the reported power handling depends on the Q of the filters. In some transmitter applications in communication systems, for example, the filters must pass powers of 10–100 W or higher. In such applications the components must pass signals while maintaining a high Q , with negligible phase and amplitude distortion for each in-band tone, and without adding spurious signals through intermodulation mixing of multiple tones. The distortion and intermodulation specifications can be particularly difficult to achieve because the high Q of many filters means that circulating RF currents greater than several amperes are often required.

The power handling of the material is described by $Z_s(H_{rf})$, where Z_s is the surface impedance and H_{rf} is the RF magnetic field at the conductor surface generated by the RF current. We have characterized $Z_s(H_{rf})$ in sputtered $\text{YBa}_2\text{Cu}_3\text{O}_{7-x}$ (YBCO) epitaxial thin films using a stripline-resonator technique at H_{rf} up to 2 kOe, at frequencies up to 20 GHz, and at temperatures from 4 K to the transition temperature T_c . Most measurements of surface resistance use a cavity resonator and are restricted to low power because of the limitations inherent in this method. The stripline, on the other hand, can generate high fields and correspondingly high power densities because of its narrow patterned center line.

All of the measured YBCO films show significant nonlinear behavior. Modeling of the measured $Z_s(H_{rf})$ has shown that the material can be described by a coupled-grain model, which is a collection of Josephson-junction weak links that are responsible for the increase in losses at high levels of RF power [1],[2]. Most important, the results of the modeling indicate that the power dependence exhibited by the films is not an intrinsic property of the material but arises from defects in the crystalline perfection. Indeed, the model predicts an intrinsic power dependence that is at least 2 orders of magnitude lower than in the best films we have measured. The estimated intrinsic power dependence, shown in Figure 7-4, will be discussed in more detail below. That the measured power dependence does not result from intrinsic properties is justification for further attempts at improvements of the film properties by refinements of the deposition conditions.

Recently, we have employed a new design [3] of an inverted cylindrical magnetron [4] sputtering system to produce YBCO films, whose current-handling capacity is improved by approximately a factor of 8 over the best reported in the past. Figure 7-4 shows $R_s(H_{rf})$ for these films at 4 K and 1.5 GHz. These

new results are compared with previously reported values obtained with films produced by off-axis magnetron sputtering. From Figure 7-4 it is clear that a substantial increase in power handling can be achieved with the cylindrical magnetron films, but we are still far from the Ginsberg-Landau intrinsic values, so greater power handling can still be achieved by improving the films. At low temperatures the surface resistance of the cylindrical magnetron films increases by only a factor of 2 for $H_{rf} = 1$ kOe, while at 77 K (not shown) this occurs for $H_{rf} = 200$ Oe.

The comparisons of power dependence among the various films are shown at 4 K rather than the more commonly used 77 K, because our measurements and modeling of the power dependence have indicated that below ~ 60 K there is little temperature dependence [2] of $R_S(H_{rf})$. The measurements and model demonstrate that

$$R_S(H_{rf}) = R_{S0}[1 + b_R(T)H_{rf}^2] , \quad (7.1)$$

where b_R is a temperature-dependent factor that results from the power dependence. Figure 7-5 presents a plot of $b_R(T)$. From the temperature dependence of b_R , we conclude that in any application where power dependence is important, operation at < 77 K (~ 60 K) is highly desirable. Since there is little change in b_R between 60 and 4 K, it is valid to make comparisons among materials at 4 K.

To examine how these results can have an impact on filters and their power-handling capability, we made some preliminary projections using filters fabricated with the new films. We have previously reported filters with a third-order intermodulation intercept point of nearly 40 dBm [5],[6], which were fabricated from films with standard power-handling capability as shown in Figure 7-4 and had transmission characteristics as presented in Figure 7-6. It should be noted that the geometry of this filter was not optimized for power handling, and while such filters are adequate in receivers they are inadequate for the transmitter applications. Based on our projections, the improved quality of the cylindrical-magnetron-sputtered films will provide about 50 times higher power-handling capability using the same geometry. This improvement is the basis of scaled filter designs that estimate > 50 -W capability using lower-impedance lines to reduce the peak current densities.

D. E. Oates	A. C. Anderson
R. W. Ralston	W. G. Lyons

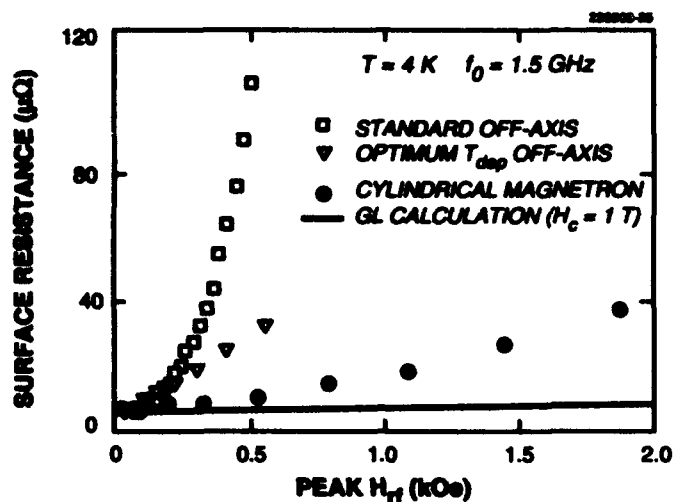


Figure 7-4. Comparison of $R_s(H_T)$ at 4 K for three YBCO films: a standard off-axis sputtered film, a film deposited with the optimum substrate temperature ($T_{dep} = 760^\circ\text{C}$), and a film deposited by cylindrical magnetron sputtering. Also shown for comparison is the estimated power dependence predicted from Ginzburg-Landau (GL) theory for a thermodynamic critical field $H_c = 1$ T.

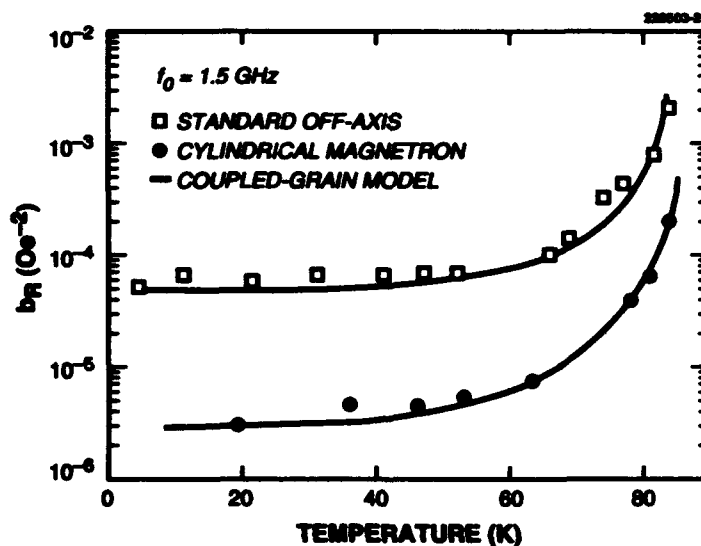


Figure 7-5. Measurements (squares and dots) and calculations (solid lines) of $b_R(T)$. The solid lines are computed using the critical current density of the Josephson junction weak links in the coupled-grain model as a free parameter to fit the data. The cylindrical magnetron films have a higher weak link critical current density than the standard off-axis films, yielding better power handling.

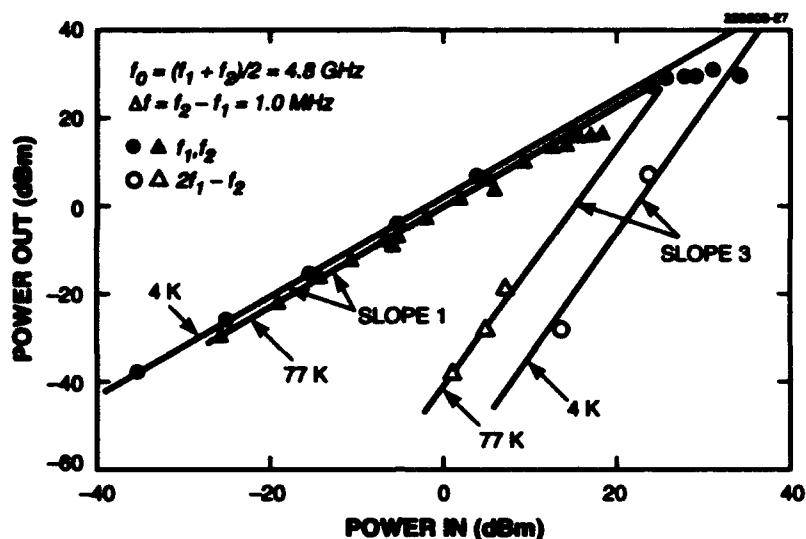


Figure 7-6. Measurements of output power vs input power showing linear response as well as one of two in-band third-order intermodulation products for a four-pole filter fabricated with YBCO film of the same quality as designated standard in Figure 7-4. The solid points are either of the essentially identical output powers of two equal-amplitude closely spaced in-band tones at frequencies f_1 and f_2 , and the open points are the output power at $2f_1 - f_2$, with circular and triangular points measured at 4 and 77 K, respectively. Solid lines are drawn to indicate slopes of 1 and 3.

REFERENCES

1. D. E. Oates, P. P. Nguyen, G. Dresselhaus, M. S. Dresselhaus, and C. C. Chin, *IEEE Trans. Appl. Superconduct.* **3**, 1114 (1993).
2. P. P. Nguyen, D. E. Oates, G. Dresselhaus, and M. S. Dresselhaus, *Phys. Rev. B* **48**, 6400 (1993).
3. A. C. Anderson, private communication.
4. J. Geerk, G. Linker, and O. Meyer, *J. Superconduct.* **5**, 345 (1992).
5. D. E. Oates, W. G. Lyons, and A. C. Anderson, *Proceedings of 45th Frequency Control Symposium* (IEEE, New York, 1991), p. 460.
6. W. G. Lyons, R. R. Bonetti, A. E. Williams, P. M. Mankiewich, M. L. O'Malley, A. C. Anderson, R. S. Withers, and R. E. Howard, *IEEE Trans. Magn.* **27**, 2537 (1991).

REPORT DOCUMENTATION PAGEForm Approved
OMB No. 0704-0188

Public reporting burden for this collection of information is estimated to average 1 hour per response, including the time for reviewing instructions, searching existing data sources, gathering and maintaining the data needed and completing and reviewing the collection of information. Send comments regarding this burden estimate or any other aspect of this collection of information, including suggestions for reducing this burden, to Washington Headquarters Services, Directorate for Information Operations and Reports, 1215 Jefferson Davis Highway, Suite 1204, Arlington, VA 22202-4302, and to the Office of Management and Budget, Paperwork Reduction Project (0704-0188), Washington, DC 20503.

1. AGENCY USE ONLY (Leave blank)

2. REPORT DATE
15 August 19933. REPORT TYPE AND DATES COVERED
Quarterly Technical Report, 1 May - 31 July 1993

4. TITLE AND SUBTITLE

Solid State Research

5. FUNDING NUMBERS

C — F19628-90-C-0002
PE — 63250F
PR — 221

6. AUTHOR(S)

Alan L. McWhorter

7. PERFORMING ORGANIZATION NAME(S) AND ADDRESS(ES)

Lincoln Laboratory, MIT
P.O. Box 73
Lexington, MA 02173-91088. PERFORMING ORGANIZATION
REPORT NUMBER

1993:3

9. SPONSORING/MONITORING AGENCY NAME(S) AND ADDRESS(ES)

HQ Air Force Materiel Command
AFMC/STSC
Wright-Patterson AFB, OH 45433-500110. SPONSORING/MONITORING
AGENCY REPORT NUMBER

ESC-TR-93-361

11. SUPPLEMENTARY NOTES

None

12a. DISTRIBUTION/AVAILABILITY STATEMENT

Approved for public release; distribution is unlimited.

12b. DISTRIBUTION CODE

13. ABSTRACT (Maximum 200 words)

This report covers in detail the research work of the Solid State Division at Lincoln Laboratory for the period 1 May through 31 July 1993. The topics covered are Electrooptical Devices, Quantum Electronics, Materials Research, Submicrometer Technology, High Speed Electronics, Microelectronics, and Analog Device Technology. Funding is provided primarily by the Air Force, with additional support provided by the Army, ARPA, Navy, SDIO, and NASA.

14. SUBJECT TERMS

electrooptical devices	high speed electronics	photorefractive effects	charge-coupled imagers
quantum electronics	microelectronics	epitaxial growth	charge-coupled correlators
materials research	analog device technology	ultraviolet lithography	superconductive films
submicrometer technology	lasers	vacuum microelectronics	

15. NUMBER OF PAGES

72

16. PRICE CODE

17. SECURITY CLASSIFICATION
OF REPORT

Unclassified

18. SECURITY CLASSIFICATION
OF THIS PAGE

Same as Report

19. SECURITY CLASSIFICATION
OF ABSTRACT

Same as Report

20. LIMITATION OF
ABSTRACT

Same as Report